

Visualizing designer quantum states in stable macrocycle quantum corrals

Jiong Lu (✉ chmluj@nus.edu.sg)

Department of Chemistry, National University of Singapore <https://orcid.org/0000-0002-3690-8235>

Xinnan Peng

Department of Chemistry, National University of Singapore

Harshitra Mahalingam

Yale-NUS College

Shaoqiang Dong

Department of Chemistry, National University of Singapore

Pingo Mutombo

Academy of Sciences of the Czech Republic

Jie Su

Department of Chemistry, National University of Singapore

Mykola Telychko

Department of Chemistry, National University of Singapore

Shaotang Song

Department of Chemistry, National University of Singapore

Pei Wen Ng

Department of Chemistry, National University of Singapore

Jishan Wu

National University of Singapore <https://orcid.org/0000-0002-8231-0437>

Pavel Jelinek

Institute of Physics of the Czech Academy of Sciences, Cukrovarnická 10, 16200 Prague 6, Czech Republic <https://orcid.org/0000-0002-5645-8542>

Chunyan Chi

Department of Chemistry, National University of Singapore

Aleksandr Rodin

National University of Singapore

Pin Lyu

Department of Chemistry, National University of Singapore

Keywords: quantum architectures, quantum technology, stable macrocycle quantum corrals, quantum states

Posted Date: June 15th, 2021

DOI: <https://doi.org/10.21203/rs.3.rs-579201/v1>

License:  This work is licensed under a Creative Commons Attribution 4.0 International License.

[Read Full License](#)

Version of Record: A version of this preprint was published at Nature Communications on October 8th, 2021. See the published version at <https://doi.org/10.1038/s41467-021-26198-8>.

Visualizing designer quantum states in stable macrocycle quantum corrals

Xinnan Peng,^{1,*} Harshitra Mahalingam,^{2,*} Shaoqiang Dong,^{1,*} Pingo Mutombo,^{3,*}
Jie Su,¹ Mykola Telychko,¹ Shaotang Song,¹ Pin Lyu,¹ Pei Wen Ng,¹ Jishan Wu,¹
Pavel Jelínek,^{3,4,†} Chunyan Chi,^{1,†} Aleksandr Rodin,^{2,5,†} and Jiong Lu^{1,5,†}

¹*Department of Chemistry, National University of Singapore, Singapore 117543, Singapore*

²*Yale-NUS College, 16 College Avenue West, Singapore 138527, Singapore*

³*Institute of Physics, Czech Academy of Sciences, Prague 16200, Czech Republic*

⁴*Regional Centre of Advanced Technologies and Materials,
Palacký University, Olomouc 78371, Czech Republic*

⁵*Centre for Advanced 2D Materials (CA2DM), National University of Singapore, Singapore 117543, Singapore*

(Dated: May 31, 2021)

Creating atomically-precise quantum architectures with high digital fidelity and desired quantum states is an important goal in a new era of quantum technology. The strategy of creating these quantum nanostructures mainly relies on atom-by-atom, molecule-by-molecule manipulation or molecular assembly through non-covalent interactions, which thus lack sufficient chemical robustness required for on-chip quantum device operation at elevated temperature. Here, we report a bottom-up synthesis of covalently linked organic quantum corrals (OQCs) with atomic precision to induce the formation of topology-controlled quantum resonance states, arising from a collective interference of scattered electron waves inside the quantum nanocavities. Individual OQCs host a series of atomic orbital-like resonance states whose orbital hybridization into artificial homo-diatomic and hetero-diatomic molecular-like resonance states can be constructed in Cassini oval-shaped OQCs with desired topologies corroborated by joint *ab initio* and analytic calculations. Our studies open up a new avenue to fabricate covalently linked large-sized OQCs with atomic precision to engineer desired quantum states with high chemical robustness and digital fidelity for new-generation quantum technology.

INTRODUCTION

Precise engineering of electron wave functions in quantum architectures has offered unprecedented opportunities to not only investigate fundamental aspects of quantum science but also to advance the technological development. The ability to create atomically-precise artificial quantum corrals with desired geometries has provided a powerful tool to explore exotic quantum phenomena such as quantum confinement [1], quantum mirage [2, 3], and quantum holograph effect [4]. Common strategies for creating artificial quantum nanostructures have mainly involved atomic manipulations and molecular assembly via non-covalent intermolecular interactions. For example, the invention of STM has offered remarkable opportunities to construct new quantum nanostructures out of just a few atoms [5–7] or molecules [8–11] on metal surfaces and directly visualize the quantum states trapped inside these nanocavities. Although tip manipulation enables the fabrication with single-atom precision, these quantum architectures assembled from adatoms or ad-molecules lack sufficient scalability. One can overcome this scalability limitation by exploiting the supramolecular self-assembly protocols that can lead to the formation of large-sized organic quantum structures assembled

via weak non-covalent intermolecular interactions [12–20]. Unfortunately, artificial quantum nanostructures created by these two methods don’t have the sufficient chemical robustness required for practical applications.

In contrast, on-surface bottom-up synthesis has revealed its remarkable potential in the fabrication of atomically precise quantum architectures [21, 22]. Implementing this approach to fabricate atomically precise covalently linked organic quantum corrals is technologically alluring as it offers high chemical stability, intrinsically digital fidelity and scalability in materials synthesis. Intensive efforts have been made to synthesize various organic rings with desired geometries and sizeable dimensions [23–26]. However, direct visualization of new quantum states living inside these organic quantum nanocavities remains elusive. This difficulty is partially due to the significant challenge of creating sizeable well-defined organic quantum corrals with dimensions comparable to the typical Fermi wavelength of surface electrons on a metallic substrate (e.g. ~ 3 nm [3, 27, 28]) to induce the “hot spot” of resonance states arising from the electron scattering due to the potential barrier produced by organic corrals. The synthesis of large-sized organic macrocycles requires delicate control over both thermodynamic and kinetic factors since competitive reaction pathways often yield different side products, and entropy effects disfavour the formation of the ordered rings [29–31].

To this end, we have devised an on-surface synthetic protocol to construct atomically precise covalently linked organic quantum corrals (OQCs) from a well-designed or-

* These authors contributed equally

† Corresponding author

ganic precursor on Au(111), with the formation of a series of new quantum resonance states, arising from a collective interference of scattered electron waves inside the OQCs. By means of scanning tunneling microscopy, we have directly visualized multiple artificial atomic orbital-like resonance states hosted in individual OQCs, whose orbital hybridization into artificial homo-diatomic and hetero-diatomic molecular-like resonance states can be constructed in OQCs with desired topologies corroborated by joint *ab initio* and analytic calculations.

RESULTS

On-surface synthesis of organic quantum corrals

The bottom-up synthetic route for the fabrication of atomically precise large-sized macrocycle as a quantum resonator involves a chemical design of precursor **1**: 4,4'-((2,6-dimethylphenyl)methylene)bis(bromobenzene). Precursor **1** is expected to undergo the thermally triggered dehydrogenation to create a radical at central methylene position, which can be delocalized to dimethylphenyl for the subsequent bonding with bromophenyl ring to form a pentagonal ring in **1'** via demethylation [32–34] (refer to the proposed mechanism in SCHEME 1). As shown in Fig. 1a, two C-Br bonds of precursor **1** with an angle of 120° are expected to facilitate the formation of a 6-unit ring based on pure geometric analysis [35]. The formation of a pentagonal ring in **1'** will enlarge the angle between these two coupling sites to around 150° (equal to the internal angle of dodecagon), thus favouring the formation of large-sized macrocycles with reduced steric-hindrance. Precursor **1** was synthesized via multiple synthetic steps (SCHEME. 2) and then deposited onto Au(111) held at room temperature under ultrahigh vacuum conditions. Subsequently, annealing of Au(111) substrate at 530 K for 20 minutes triggers the surface-assisted coupling reactions towards the formation of linear polymeric chains, curved ring segments, and perfect 12-unit circular polymer rings (Fig. 1b). Statistical distribution of these curved ring segments and complete 12-unit rings *via* analysis of multiple STM images (Fig. S1) reveals that the yield of curved ring segments tends to be lower with an increase of the number of building units but exhibits one local maximum for the 12-unit rings (2.5%). DFT calculations reveal that the formation energy divided by the number (n) of building units decreases for $6 \leq n \leq 12$, while increases for $n \geq 12$. It is noted that a minimum value occurs at $n = 12$ in the plot of formation energies divided by n (Fig. 1c), suggesting that the generation of symmetric 12-unit rings is energetically favourable. A delicate control over the interplay between thermodynamic and kinetic factors may allow for achieving a higher yield of the

symmetric 12-unit ring [29–31].

An STM image of the symmetric 12-unit ring acquired by a metallic tip resolves a sunflower-like topology with a pore of 3.86 nm in diameter (Fig. 1b,c). In addition, we also performed bond-resolved STM (BR-STM) imaging using a carbon monoxide functionalized tip (CO-tip) to resolve the internal molecular backbone structure of this macrocycle [21, 36–39]. The BR-STM imaging was conducted in constant height mode in the Pauli repulsion regime, wherein the CO molecule undergoes a lateral relaxation over the areas with a high electron density (chemical bond), which modulates the overall conductance in the tunnelling junction, yielding sharp features associated with the chemical bond in the tunnelling current channel [40–42]. The corresponding BR-STM image of this macrocycle reveals interconnected 12 triangular-shaped monomers (Fig. 2a), wherein each building unit contains one pentagonal ring resulting from the demethylation of precursor **1** as discussed above. The formation of a pentagonal ring in the building unit breaks the structural symmetry and results in the formation of one zigzag side (ZS) and one pentagon-decorated side (PS). It is noted that the majority of monomers tend to connect at the same side (ZS or PS) with neighboring monomers (Fig. 1a). We also noted that one or a few of monomers in such a 12-unit macrocycle might show the reversed arrangement of ZS and PS sides due to the presence of two possible demethylation sides (Fig. 2a). However, such a structural variation in these isomers shows a negligible variation in the energy positions of frontier orbitals and associated energy gap of 12-unit macrocycles (Fig. 2c and Fig. S4a). The large-sized 12-unit macrocycles with a circular potential profile are expected to act as organic quantum corrals (12-OQC) to engineer the designer quantum resonance states. In addition, the covalently bonded nature of 12-OQC exhibits high chemical robustness and stability against thermal- or tip-induced diffusion (often occurring in the adatom-derived quantum corrals), making it an ideal candidate to serve as a robust quantum corral.

Electronic structure of organic corrals

To probe its electronic structure, we performed differential conductance spectroscopy (dI/dV) measurement over the 12-OQC on Au(111). Fig. 2c presents the corresponding dI/dV spectra collected over the pentagonal ring (blue curve) and the inner edge (red curve) of 12-OQC, along with the reference spectrum recorded on bare Au(111) (grey dashed curve). The dI/dV spectrum collected at the pentagonal ring shows two pronounced peaks at $+1.3 \pm 0.05$ V and $+1.8 \pm 0.05$ V. In addition, two adjacent peaks at -1.05 ± 0.05 V and -1.45 ± 0.05 V appear in the dI/dV spectrum acquired at the inner edge of 12-OQC. We further probed the spatial distribu-

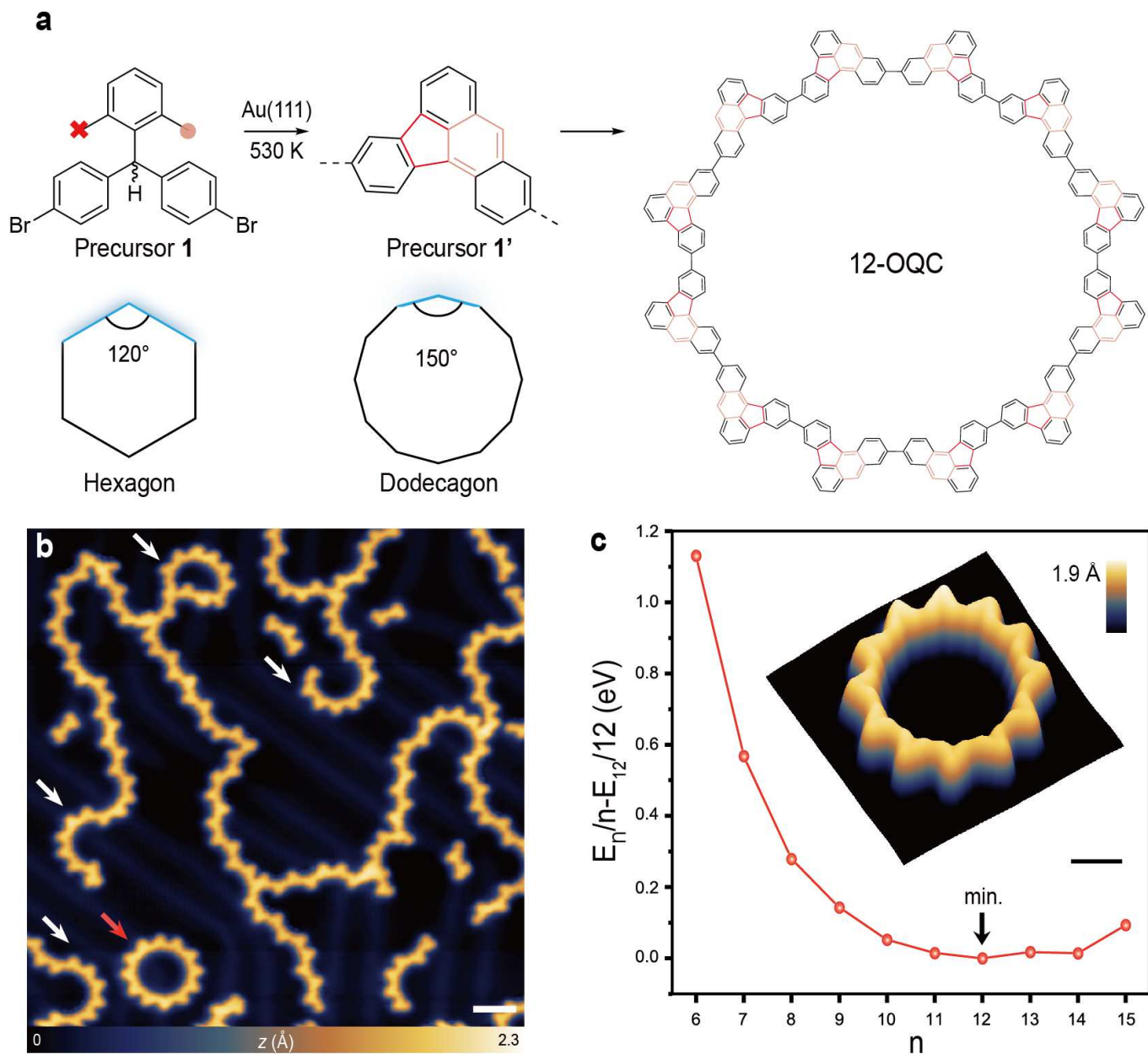


FIG. 1. **On-surface synthesis of covalently linked macrocycles.** **a**, Schematic illustrating the synthetic pathway from precursor (left) to the 12-unit macrocycle (right) with a proposed intermediate (Precursor 1') with embedded pentagonal ring (middle). **b**, Overview STM image after annealing Precursor 1 on Au(111) at 530 K, revealing individual 12-unit macrocycle (one of them is highlighted with a red arrow) coexisting with curved segments or half rings (highlighted with white arrows) and polymer chains ($V = 1.0$ V, $I = 200$ pA). **c**, Plot of energy differences between total energy divided by number of units and the reference energy of 12-unit macrocycle. Inset shows the three-dimensional STM image of one 12-unit macrocycle ($V = -0.1$ V, $I = 200$ pA). The scale bars in **b** and **c** are 3 nm and 1 nm, respectively

185 tion of these molecular states via dI/dV mapping with¹⁹²
 186 a metal tip. The dI/dV maps (Fig. 2d,e) collected at¹⁹³
 187 the corresponding energies of -1.05 V and $+1.3$ V re¹⁹⁴
 188 reveal the characteristic nodal patterns predominantly lo¹⁹⁵
 189 calized at both inner and outer edges, which can be as¹⁹⁶
 190 signed to the valence band (CB) and conduction band¹⁹⁷
 191 (VB), respectively. DFT calculations of a freestanding¹⁹⁸

12-OQC reveal three nearly degenerate frontier orbitals
 for both filled and empty states, which yield a band-like
 electronic structure of this macrocycle (the wave func-
 tions of the corresponding frontier orbitals are shown in
 Fig. S3). The calculated dI/dV maps with an s -wave
 tip (Fig. 2f,g) show good agreement with experimental
 patterns observed for VB and CB, respectively. Both ex-

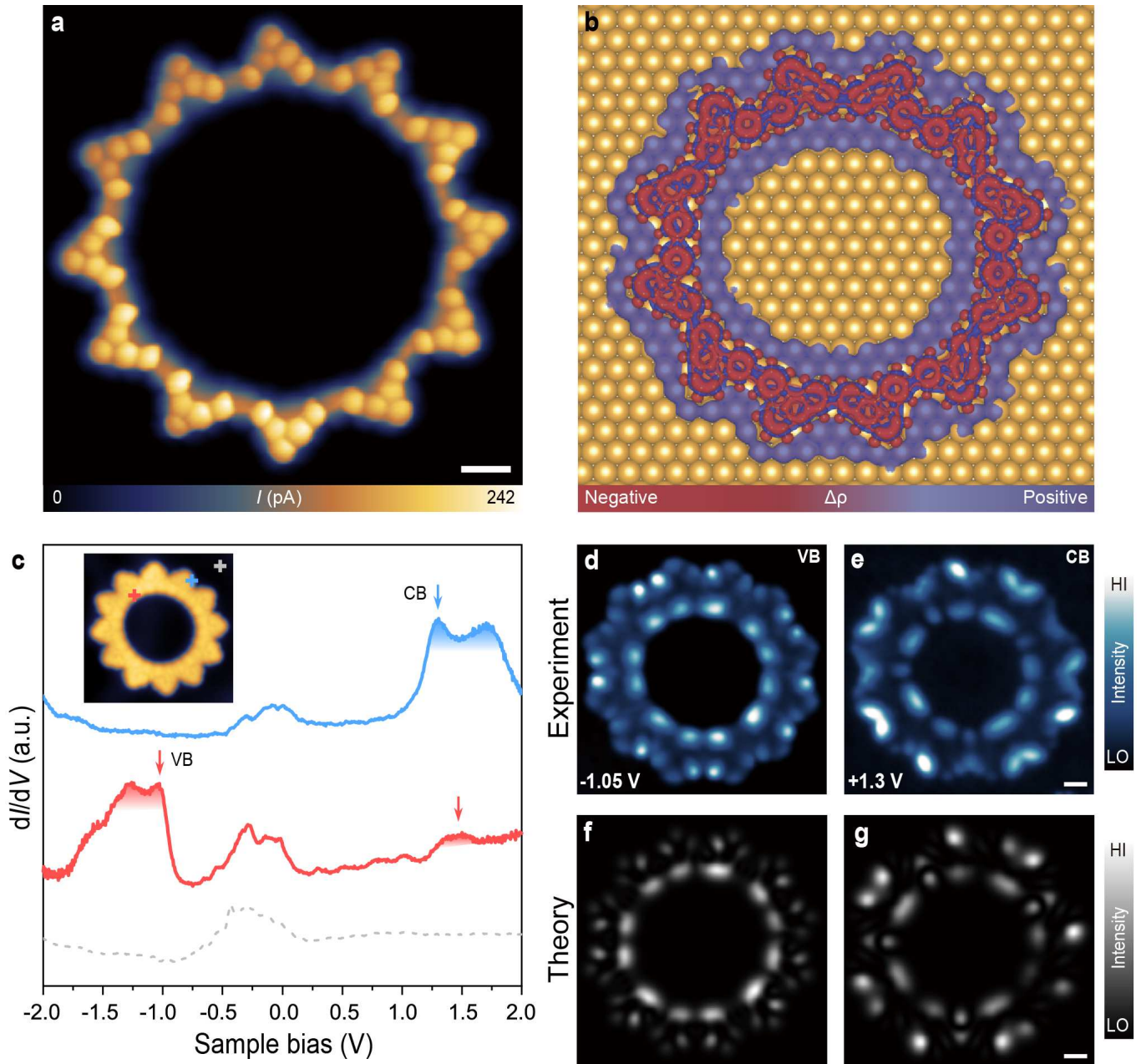


FIG. 2. **Structural and electronic structure characterization of 12-OQC.** **a**, Corresponding BR-STM image ($V = 3$ mV, $\Delta z = -1.2$ Å; set point prior to turn off feedback, $V = 20$ mV, $I = 600$ pA). **b**, 3D isosurface of the electronic density differences with an isovalue of ± 0.001 e/Å³ of 12-OQC on Au(111) surface. Red and purple regions in 3D plots represent charge depletion and accumulation, respectively. **c**, Point dI/dV spectra acquired over different sites of 12-OQC and Au(111) substrate. dI/dV curves taken at the pentagonal ring (blue curve), inner edge of 12-OQC (red curve), and taken on Au(111) (grey dashed curve). **d,e**, Constant-current dI/dV maps recorded at the energy positions of the VB (-1.05 V) and CB ($+1.3$ V) of 12-OQC, respectively ($I = 2$ nA for **d,e**). **f,g**, Simulated dI/dV maps acquired at different energy positions corresponding to different sets of orbitals: **f**: ψ_{1-3} , **g**: ψ_{4-6} . Scale bar: 5 Å.

199 perimental and theoretical dI/dV plots reveal a stronger
 200 intensity localized at the ZS and PS for CB and VB,
 201 respectively. In addition, we also performed the dI/dV
 202 measurements over another 12-OQC ring with slightly
 203 different internal arrangement of building units as shown
 204 in Fig. S4, which reveal the energetic positions of CB and

VB similar to that of the 12-OQC shown in Fig. 2. Therefore, electronic structures of 12-OQC show a negligible variation even in the presence of misaligned monomers with the opposite ZS/PS arrangement in these macrocycles, which renders them as robust OQCs with high digital fidelity to confine the surface electrons into a series

of quantum resonance states as discussed below.

Quantum resonance states in the Cassini oval-shaped OQCs

Quantum resonance states in the 12-OQC

Interfacial charge redistribution often occurs between molecular adsorbents and metallic surfaces [43, 44], resulting in local potential variation over the macrocycle compared to the bare surface. Our DFT calculations also reveal that the charge redistribution leads to the formation of a circular negative potential profile at the organic backbone (Fig. 2b and Fig. S2) that can induce scattering of surface electrons, leading to the formation of quantum states. We then performed dI/dV measurements to probe the energy-dependent local density of states (LDOS) inside 12-OQC. As shown in Fig. 3a, the dI/dV spectrum (blue curve) acquired at the centre of 12-OQC reveals additional features including a sharp peak at -0.26 ± 0.05 V (labelled as P_1), and two broad peaks centred at $+0.46 \pm 0.1$ V (labelled as P_3) and $+1.56 \pm 0.1$ V (labelled as P_5). Moreover, the dI/dV spectrum (red curve) acquired 0.75 nm away from the centre reveals another resonance state at $+0.91 \pm 0.1$ V (labelled as P_4). In addition, a weak resonance at $+40 \pm 20$ mV (labelled as P_2) along with molecular CB state were revealed in the spectrum (orange curve) acquired near the inner edge of 12-OQC (1.25 nm away from the centre of 12-OQC). We then carried out dI/dV mapping to probe the spatial distribution of these new electronic states inside the ring. As shown in Fig. 3d, the P_1 state exhibits a dome-like pattern inside the 12-OQC, in contrast to the dark region right over the 12-OQC at the same sample bias. The P_3 state displays a bright dot surrounded by a dark ring, concentrically followed by a bright ring merging with the inner edge of 12-OQC (which can be seen more clearly in simulated spectral function maps in Fig. 3i-k). The dI/dV map of the P_5 state is characterized by a protrusion in the centre concentrically surrounded by a darker inner and brighter outer ring-like feature. In addition, the dotted pattern observed over the ring at this sample bias is energetically close to that of CB can be assigned to the contribution from the CB state of 12-OQC. Moreover, the dI/dV map of the P_4 state reveals a doughnut-shaped pattern. Unfortunately, the spatial distribution of the P_2 state cannot be resolved clearly by dI/dV mapping at constant current mode near Fermi energy due to the presence of molecular topographical variation (Fig. S6). The P_2 state can be expected to exhibit a doughnut-shaped pattern (similar to that of P_4 state) located near the inner edge of 12-OQC as evidenced from the 2D contour plot of dI/dV spectra acquired across the pore of 12-OQC (Fig. 3b).

We also observed the formation of regular Cassini oval-shaped OQC (COS-OQC) (Fig. 4a), which can be viewed as two 6-unit half rings connected by two monomer linkers pointing to the centre, as verified by the corresponding BR-STM image (Fig. S7). The COS-OQC with an open channel at the centre allows for the strong electronic coupling between adjacent quantum states which otherwise live in two isolated half-rings. Such a desired topology with electronic coupling is expected to mimic the orbital hybridization effect in homo-diatomic molecules. Unlike isolated 12-OQC, a pair of electronic states (Fig. 4b) were observed at -0.32 ± 0.05 V and -0.18 ± 0.05 V, predominately located at the neck of COS-OQC (blue cross) and the centre of two half rings (red cross), respectively. dI/dV maps acquired at the energies corresponding to these two emerging electronic states reveal that the low energy state (-0.32 V) (Fig. 4e) has an oval shape with stronger intensity localized at the neck of COS-OQC. In contrast, the high energy state (-0.18 V) (Fig. 4f) shows an hourglass-like shape with stronger intensity localized at the centre of half rings with a node pattern at the neck. Such a spatial pattern resembles the characteristic bonding and anti-bonding states of H_2 -like molecular orbitals, which is presumably due to the orbital hybridization between adjacent quantum states in two coupled half rings. This will be further discussed in the next section.

DISCUSSION

Probing the origin of quantum resonance states in OQCs

Introducing any perturbation to a 2D electron gas system breaks the translational invariance, giving rise to a position-dependent LDOS. In this study, the gold surface states are perturbed by OQCs. To investigate the nature of such a perturbation, we first performed *ab initio* calculations, demonstrating that there is virtually no direct charge transfer between gold and 12-OQC. However, the orbital repulsion between the two components forms an interfacial dipole between the nanoring and the metallic substrate [43, 44], resulting in a short-range repulsive potential to which the surface electrons respond (Fig. 2b and Fig. S2).

Despite the presence of a circular potential barrier resembling a 2D well, this system does not contain bound states, which can be understood as follows. The potential profile experienced by the surface electrons is limited to the region right below the OQC. The potential inside the OQC is identical to that outside, which can be set to zero. Hence, for an electron inside the corral, the corral

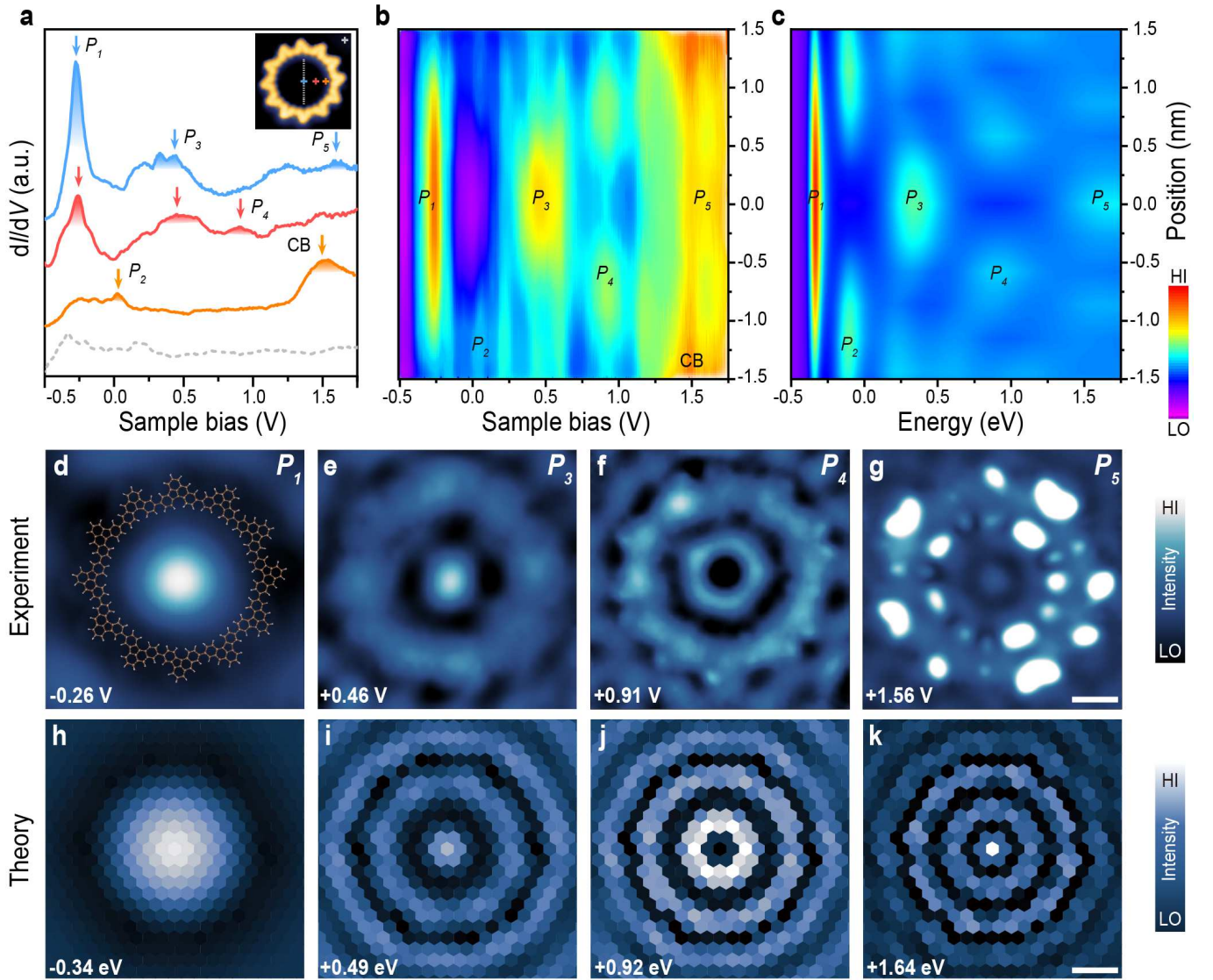


FIG. 3. Characterization of quantum resonance states trapped in a 12-OQC. **a**, Point dI/dV spectra acquired over different sites inside a 12-OQC and Au(111) substrate. dI/dV curves taken at the centre (blue curve), 0.75 nm away from the centre of 12-OQC (red curve), 1.25 nm away from the centre of 12-OQC (orange curve), and taken on Au(111) (grey dashed curve). **b**, Color-coded dI/dV spectra (spaced by 0.15 nm) taken across the pore of 12-OQC. The actual positions where the dI/dV spectra were taken are indicated by gray dots in the inset STM image in **a**. **c**, Color-coded simulated spectral function curves (spaced by 0.15 nm) taken across the pore of potential corral in gold unit cells (Fig. S11). **d-g**, Constant-current dI/dV maps recorded at different energy positions ($I = 1$ nA for **d**, **e**; $I = 1.5$ nA for **f**, **g**). Panels **d-g** refer to the P_1 (-0.26 V), P_3 ($+0.46$ V), P_4 ($+0.91$ V), and P_5 ($+1.56$ V) of resonance states, respectively (The chemical structure of 12-OQC is superimposed on panel **d** to indicate its position). **h-k**, Simulated spectral function maps acquired at different energy positions close to the energetic positions of these quantum resonance states observed experimentally. Panels **h-k** refer to the P_1 (-0.34 eV), P_3 ($+0.49$ eV), P_4 ($+0.92$ eV), and P_5 ($+1.64$ eV) of resonance states, respectively. Scale bar: 1 nm.

313 boundary represents a potential barrier with finite width³²¹
 314 and height between two regions of equal potential. This³²²
 315 barrier structure guarantees a finite tunnelling probab-³²³
 316 ity for the electron, in contrast to a bound state with an³²⁴
 317 infinite lifetime. In fact, solving the Schrödinger equation³²⁵
 318 for a 2D parabolic dispersion with such a barrier does³²⁶
 319 not yield solutions that decay exponentially outside the³²⁷
 320 corral. Instead, one obtains radially propagating Bessel³²⁸

functions, representing free states. Moreover, the model of bound states cannot be used to explain the standing wave patterns (Fig. S9) outside the potential barrier where the surface electrons are totally free.

Although the corral does not produce true confined states, it does give rise to resonances, which can be viewed as hybridizations of true bound states of a circular well with the free-propagating surface electrons [45]. The

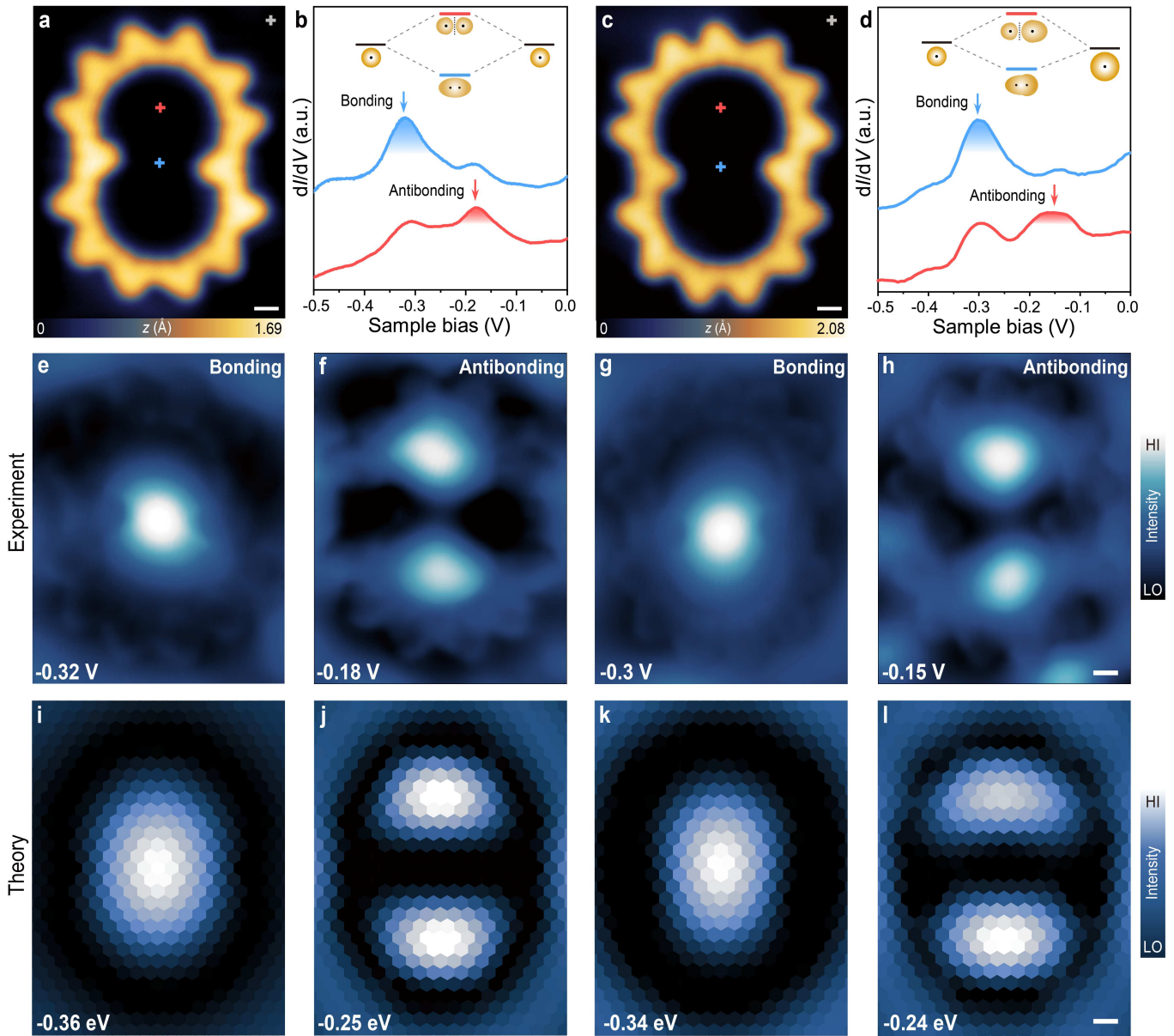


FIG. 4. **Characterization of coupled quantum resonance states in COS-OQCs.** **a**, STM image of a symmetric COS-OQC ($V = -0.32$ V, $I = 1.5$ nA). **b**, Point dI/dV spectra acquired over different sites inside a symmetric COS-OQC and Au(111) substrate. dI/dV curves taken at the neck (blue curve) and 1.23 nm away from the neck of symmetric COS-OQC (red curve). **c**, STM image of an asymmetric COS-OQC ($V = -0.3$ V, $I = 1.5$ nA). **d**, Point dI/dV spectra acquired over different sites inside an asymmetric COS-OQC and Au(111) substrate. dI/dV curves taken at the neck (blue curve) and 1.4 nm away from the neck of an asymmetric COS-OQC (red curve). **e,f**, Constant-current dI/dV maps recorded at different energy positions over a symmetric COS-OQC ($I = 1$ nA for **e,f**). Panels **e,f** refer to the bonding (-0.32 V) and antibonding (-0.18 V) states, respectively. **g,h**, Constant-current dI/dV maps recorded at different energy positions over an asymmetric COS-OQC ($I = 1$ nA for **g,h**). Panels **g,h** refer to the bonding (-0.3 V) and antibonding (-0.15 V) states, respectively. **i,j**, Simulated spectral function maps of a symmetric COS-OQC acquired at different energy positions corresponding to bonding (-0.36 eV) and antibonding states (-0.25 eV), respectively. **k,l**, Simulated spectral function maps of an asymmetric COS-OQC acquired at different energy positions corresponding to bonding (-0.34 eV) and antibonding states (-0.24 eV), respectively. Scale bar: 5 Å.

329 greater the barrier produced by the corral, the weaker
 330 the tunnelling (hybridization) and the more the elec-
 331 tronic density inside the corral resembles the confined
 332 states (Fig. S10). We, therefore, can describe the forma-

tion of these new quantum resonance states in 12-OQC
 and COS-OQC within an electron scattering potential
 framework, which employs nearly-free electron model to
 describe the surface states of Au(111). This approach

yields a 2D isotropic parabolic dispersion with an effective electronic mass of $0.27 m_e$ [46, 47], where m_e is the mass of an electron, and the Fermi energy is located at 0.46 eV above the band minimum [48, 49].

To include the local potential variation, we first partition the gold surface into a grid of unit cells, each hosting a single orbital of the single-band model. We then include a positive (repulsive) potential term for the unit cells influenced by the dipole from OQCs. Because the dipole potential decays quickly with distance, we only include it for the unit cells directly under OQC (Fig. S11). The repulsive potential contour generated by a OQC produces a “corral” for surface electrons.

Introducing a point-like potential perturbation to a metallic system with isotropic dispersion creates the well-known Friedel oscillations in the electronic density with the period determined by the Fermi momentum k_F [50–52]. Moreover, electrons at each momentum $k < k_F$ also produce oscillations in the density with longer wavelengths which can be visualized experimentally in dI/dV maps [53]. Including multiple scatterers in the system produces interference, which can be treated as a superposition of the scattering patterns from each point scatterer considered individually. Alternatively, one can employ a non-perturbative approach and calculate the resultant density variation for a collection of scatterers simultaneously. In this study, we make use of the latter approach as discussed in the Supplementary Information.

To compare theoretical results to the experimental data, we first “draw” the corral of the appropriate shape by introducing local repulsive potential to the gold unit cells located below the OQC. Next, we calculate the position-dependent spectral function following the procedure described in Supplementary Information (**Analytical Theory**). The spectral function gives the density of states at a particular unit cell at a given energy. Because the differential conductance at some bias V is related to the number of states available for tunnelling at that energy, we use the spectral function as a proxy for the dI/dV data. By fixing the energy at which the spectral function is computed, it is possible to obtain spectral function spatial maps like the ones shown in Fig. 3h-k and Fig. 4i-l. On the other hand, if the position is kept constant, varying the energy yields the dI/dV -like curves (Fig. S5), corresponding to horizontal slices of Fig. 3c. Because of the generality of our formalism, we can study the highly symmetric circular OQC and the more challenging COS-OQC.

The spectral function depends on the electronic dispersion and the scattering potential. Assuming that the potential produced by OQC is restricted to the region directly below the polymer, our theoretical treatment only requires a single fitting parameter: the magnitude of this potential because we already know the effective mass of the surface-state electrons. As was discussed above, the greater the potential barrier separating the interior of

the OQC from the rest of the surface, the more the resonances resemble the true bound states. Reducing the potential broadens the states, as shown in Fig. S10.

With a repulsive potential of 0.6 eV, the simulated spectral function curves and 2D contour plot of spectral function curves (Fig. 3c) show good agreement with experimental data. Such a value, lower than the typical amount of charge transferred in the molecular systems with the occupation and depletion of molecular states, can therefore be rationalized in our system only with interfacial charge polarization, consistent with our DFT predictions. We also noticed several mild discrepancies between experimental dI/dV data (Fig. 3b) and the theoretical simulations (Fig. 3c). First, at the high sample bias (~ 1.5 V), the experimental results contain the signature of the CB of 12-OQC that is not included in the theoretical model. Additionally, the peaks in the experimental data are shifted towards slightly higher bias compared to the theoretical ones. This mild quantitative disagreement is not unexpected because, as was stated above, the spectral function is a proxy for the dI/dV signal with the latter depending also on the electronic convolution with the tip. The key features, such as the dI/dV peaks and the oscillating signal rings in the dI/dV maps, however, are robust and show good agreement between theory and experiment.

Next, we discuss the hybridization phenomenon in COS-OQCs. The two-dimensional electron gas (2DEG) with discrete resonance states could be viewed as an artificial “hydrogen atom” constructed by the circular corral. In principle, artificial homo-diatom H₂-like molecular orbitals can be realized in COS-OQC, wherein two adjacent “H atoms” can undergo orbital hybridization. Firstly, the energy halfway between the two emerging electronic states in COS-OQC (-0.25 eV) is close to the energy position of P_1 state (-0.26 eV) in a 12-OQC because of their comparable diameters. It could be envisioned that the original “atomic” orbitals constructed in the two half rings with open neck channel can effectively hybridize and split into one bonding state at lower energy and one antibonding state at higher energy (inset of Fig. 4b), analogous to the hybridization of two neighbouring resonance states arising from vacancies in molecular self-assembly [54]. The theoretical results, shown in Fig. 4i-j, exhibit a very similar behavior with the energies of the single-hot spot and the hourglass-like states sandwiching the P_1 peak of the circular OQC.

In addition, we also investigated an asymmetric COS-OQC including a larger half-ring with one more monomer than an adjacent smaller half ring (Fig. 4c). In this case, an artificial “hetero-diatom molecule” would be constructed due to the energy level mismatch between the original “atomic” orbitals from the two half rings with different sizes. One pair of bonding (-0.3 V)/antibonding (-0.15 V) states and their corresponding dI/dV maps are shown in Fig. 4d,g,h, respectively.

It is noted that the bonding and antibonding states show asymmetric spatial distribution in the two half rings which agree with the theoretical results in Fig. 4k-l. Therefore, an artificial giant “homo-diatom molecule” and “hetero-diatom molecule” can be constructed by engineering the topology of OQCs. Moreover, the tip manipulation can be used to close and open up the OQC to engineer multiple quantum resonance states by controlling their dimensions and geometries (Fig. S12). A series of resonance states with hot-spots and ring-like patterns were revealed by dI/dV measurements of the irregular rings before and after tip manipulation. As expected, we also observed that these resonance states shift towards higher energy positions as the ring is closed up by tip manipulation, equivalent to the reduction of the lateral dimensions of the OQCs. This opens up virtually unlimited opportunities for engineering the desired quantum resonance states inside chemically robust organic quantum corrals.

CONCLUSION

In summary, we have demonstrated a bottom-up atomically precise synthesis of chemically robust OQCs with topology-controlled new quantum resonance states, arising from a collective interference of scattered electron waves inside the quantum corrals. Individual OQCs with a series of resonance states behave like artificial atomic orbitals. The effective coupling of artificial atomic orbitals leads to the formation of artificial homo-diatom and hetero-diatom molecular states in OQCs with desired topologies corroborated by a joint *ab initio* and analytical calculations. The fabrication of covalently linked large-sized OQCs with atomic precision not only grants access into the quantum nature of these systems with intrinsically digital fidelity but also enables the precise engineering of desired quantum states with high chemical robustness for technological applications ranging from nanophotonics to quantum information processing.

[1] M. F. Crommie, C. P. Lutz, and D. M. Eigler, *Science* **262**, 218 (1993).
 [2] H. C. Manoharan, C. P. Lutz, and D. M. Eigler, *Nature* **403**, 512 (2000).
 [3] G. A. Fiete and E. J. Heller, *Reviews of Modern Physics* **75**, 933 (2003).
 [4] C. R. Moon, L. S. Mattos, B. K. Foster, G. Zeltzer, and H. C. Manoharan, *Nature Nanotechnol.* **4**, 167 (2009).
 [5] E. J. Heller, M. F. Crommie, C. P. Lutz, and D. M. Eigler, *Nature* **369**, 464 (1994).
 [6] K. F. Braun and K. H. Rieder, *Phys. Rev. Lett.* **88**, 096801 (2002).
 [7] F. Stilp, A. Bereczuk, J. Berwanger, N. Mundigl, K. Richter, and F. J. Giessibl, *Science*, eabe2600 (2021).

[8] C. R. Moon, L. S. Mattos, B. K. Foster, G. Zeltzer, W. Ko, and H. C. Manoharan, *Science* **319**, 782 (2008).
 [9] K. K. Gomes, W. Mar, W. Ko, F. Guinea, and H. C. Manoharan, *Nature* **483**, 306 (2012).
 [10] S. Paavilainen, M. Ropo, J. Nieminen, J. Akola, and E. Räsänen, *Nano Lett.* **16**, 3519 (2016).
 [11] M. R. Slot, T. S. Gardenier, P. H. Jacobse, G. C. Van Miert, S. N. Kempkes, S. J. Zevenhuizen, C. M. Smith, D. Vanmaekelbergh, and I. Swart, *Nat. Phys.* **13**, 672 (2017), arXiv:1611.04641.
 [12] F. Klappenberger, D. Kühne, W. Krenner, I. Silanes, A. Arnau, F. De Javier García Abajo, S. Klyatskaya, M. Ruben, and J. V. Barth, *Nano Lett.* **9**, 3509 (2009).
 [13] J. Lobo-Checa, M. Matena, K. Müller, J. H. Dil, F. Meier, L. H. Gade, T. A. Jung, and M. Stöhr, *Science* **325**, 300 (2009).
 [14] F. Klappenberger, D. Kühne, W. Krenner, I. Silanes, A. Arnau, F. J. García De Abajo, S. Klyatskaya, M. Ruben, and J. V. Barth, *Phys. Rev. Lett.* **106**, 026802 (2011).
 [15] J. Wyrick, D. H. Kim, D. Sun, Z. Cheng, W. Lu, Y. Zhu, K. Berland, Y. S. Kim, E. Rotenberg, M. Luo, P. Hyldgaard, T. L. Einstein, and L. Bartels, *Nano Lett.* **11**, 2944 (2011).
 [16] S. Wang, W. Wang, L. Z. Tan, X. G. Li, Z. Shi, G. Kuang, P. N. Liu, S. G. Louie, and N. Lin, *Phys. Rev. B* **88**, 245430 (2013).
 [17] N. Kepčija, T. J. Huang, F. Klappenberger, and J. V. Barth, *J. Chem. Phys.* **142**, 101931 (2015).
 [18] K. Müller, M. Enache, and M. Stöhr, *J. Phys.: Condens. Matter* **28**, 153003 (2016).
 [19] Y. Q. Zhang, J. Björk, J. V. Barth, and F. Klappenberger, *Nano Lett.* **16**, 4274 (2016).
 [20] I. Piquero-Zulaica, J. Lobo-Checa, A. Sadeghi, Z. M. El-Fattah, C. Mitsui, T. Okamoto, R. Pawlak, T. Meier, A. Arnau, J. E. Ortega, J. Takeya, S. Goedecker, E. Meyer, and S. Kawai, *Nature Commun.* **8**, 787 (2017).
 [21] J. Su, W. Fan, P. Mutombo, X. Peng, S. Song, M. Ondráček, P. Golub, J. Brabec, L. Veis, M. Telychko, P. Jelínek, J. Wu, and J. Lu, *Nano Lett.* **21**, 861 (2021).
 [22] M. Telychko, G. Li, P. Mutombo, D. Soler-Polo, X. Peng, J. Su, S. Song, M. J. Koh, M. Edmonds, P. Jelínek, J. Wu, and J. Lu, *Sci. Adv.* **7**, eabf0269 (2021).
 [23] Q. Fan, C. Wang, Y. Han, J. Zhu, W. Hieringer, J. Kuttner, G. Hilt, and J. M. Gottfried, *Angewandte Chemie - International Edition* **52**, 4668 (2013).
 [24] A. Summerfield, M. Baldoni, D. V. Kondratuk, H. L. Anderson, S. Whitelam, J. P. Garrahan, E. Besley, and P. H. Beton, *Nature Commun.* **10**, 2932 (2019).
 [25] K. Kaiser, L. M. Scriven, F. Schulz, P. Gawel, L. Gross, and H. L. Anderson, *Science* **365**, 1299 (2019).
 [26] C. Fan, B. Sun, Z. Li, J. Shi, T. Lin, J. Fan, and Z. Shi, *Angewandte Chemie International Edition* **60**, 1 (2021).
 [27] F. Reinert, G. Nicolay, S. Schmidt, D. Ehm, and S. Hüfner, *Phys. Rev. B* **63**, 115415 (2001).
 [28] S. D. Kevan and R. H. Gaylord, *Phys. Rev. B* **36**, 5809 (1987).
 [29] M. Liu, S. Li, J. Zhou, Z. Zha, J. Pan, X. Li, J. Zhang, Z. Liu, Y. Li, and X. Qiu, *ACS Nano* **12**, 12612 (2018).
 [30] M. Fritton, D. A. Duncan, P. S. Deimel, A. Rastgoolahrood, F. Allegretti, J. V. Barth, W. M. Heckl, J. Björk, and M. Lackinger, *J. Am. Chem. Soc.* **141**, 4824 (2019).

- [31] C. K. Krug, D. Nieckarz, Q. Fan, P. Szabelski, and J. M. Gottfried, *Chem. Eur. J.* **26**, 7647 (2020).
- [32] Y. Zheng, C. Li, C. Xu, D. Beyer, X. Yue, Y. Zhao, G. Wang, D. Guan, Y. Li, H. Zheng, C. Liu, J. Liu, X. Wang, W. Luo, X. Feng, S. Wang, and J. Jia, *Nature Commun.* **11**, 6076 (2020).
- [33] Y. Zheng, C. Li, Y. Zhao, D. Beyer, G. Wang, C. Xu, X. Yue, Y. Chen, D. D. Guan, Y. Y. Li, H. Zheng, C. Liu, W. Luo, X. Feng, S. Wang, and J. Jia, *Phys. Rev. Lett.* **124**, 147206 (2020).
- [34] S. Mishra, D. Beyer, R. Berger, J. Liu, O. Gröning, J. I. Urgel, K. Müllen, P. Ruffieux, X. Feng, and R. Fasel, *J. Am. Chem. Soc.* **142**, 1147 (2020).
- [35] C. Steiner, J. Gebhardt, M. Ammon, Z. Yang, A. Heidenreich, N. Hammer, A. Görling, M. Kivala, and S. Maier, *Nature Commun.* **8**, 14765 (2017).
- [36] G. D. Nguyen, H. Z. Tsai, A. A. Omrani, T. Marangoni, M. Wu, D. J. Rizzo, G. F. Rodgers, R. R. Cloke, R. A. Durr, Y. Sakai, F. Liou, A. S. Aikawa, J. R. Chelikowsky, S. G. Louie, F. R. Fischer, and M. F. Crommie, *Nature Nanotechnol.* **12**, 1077 (2017).
- [37] J. Li, N. M. Díez, E. C. Sanromà, M. Vilas-Varela, D. G. De Oteyza, D. Peña, M. Corso, and J. I. Pascual, *Sci. Adv.* **4**, eaaq0582 (2018).
- [38] J. Li, S. Sanz, J. Castro-Esteban, M. Vilas-Varela, N. Friedrich, T. Frederiksen, D. Peña, and J. I. Pascual, *Phys. Rev. Lett.* **124**, 177201 (2020).
- [39] S. Song, N. Guo, X. Li, G. Li, Y. Haketa, M. Telychko, J. Su, P. Lyu, Z. Qiu, H. Fang, X. Peng, J. Li, X. Wu, Y. Li, C. Su, M. J. Koh, J. Wu, H. Maeda, C. Zhang, and J. Lu, *J. Am. Chem. Soc.* **142**, 13550 (2020).
- [40] P. Hapala, G. Kichin, C. Wagner, F. S. Tautz, R. Temirov, and P. Jelínek, *Phys. Rev. B* **90**, 085421 (2014), arXiv:1406.3562.
- [41] P. Hapala, R. Temirov, F. S. Tautz, and P. Jelínek, *Phys. Rev. Lett.* **113**, 226101 (2014), arXiv:1409.3405.
- [42] O. Krejčí, P. Hapala, M. Ondráček, and P. Jelínek, *Phys. Rev. B* **95**, 045407 (2017), arXiv:1609.09462.
- [43] H. Ishii, K. Sugiyama, E. Ito, and K. Seki, *Adv. Mater.* **11**, 605 (1999).
- [44] S. Braun, W. R. Salaneck, and M. Fahlman, *Energy-level alignment at organic/metal and organic/organic interfaces* (2009).
- [45] G. D. Mahan, *Many-Particle Physics*, Physics of Solids and Liquids (Springer US, 2000).
- [46] W. Chen, V. Madhavan, T. Jamneala, and M. F. Crommie, *Phys. Rev. Lett.* **80**, 1469 (1998).
- [47] L. Bürgi, H. Brune, and K. Kern, *Phys. Rev. Lett.* **89**, 176801 (2002).
- [48] K. Schouteden, E. Lijnen, E. Janssens, A. Ceulemans, L. F. Chibotaru, P. Lievens, and C. Van Haesendonck, *New J. Phys.* **10**, 43016 (2008).
- [49] K. Schouteden, P. Lievens, and C. Van Haesendonck, *Phys. Rev. B* **79**, 195409 (2009).
- [50] Y. Hasegawa and P. Avouris, *Phys. Rev. Lett.* **71**, 1071 (1993).
- [51] L. Petersen, P. Laitenberger, E. Lægsgaard, and F. Besenbacher, *Phys. Rev. B* **58**, 7361 (1998).
- [52] L. Petersen, P. T. Sprunger, P. Hofmann, E. Lægsgaard, B. G. Briner, M. Doering, H.-P. Rust, A. M. Bradshaw, F. Besenbacher, and E. W. Plummer, *Phys. Rev. B* **57**, R6858 (1998).
- [53] L. Gross, F. Moresco, L. Savio, A. Gourdon, C. Joachim, and K. H. Rieder, *Phys. Rev. Lett.* **93**, 056103 (2004).
- [54] K. Seufert, W. Auwärter, F. J. García De Abajo, D. Ecija, S. Vijayaraghavan, S. Joshi, and J. V. Barth, *Nano Lett.* **13**, 6130 (2013).
- [55] J. P. Lewis, P. Jelínek, J. Ortega, A. A. Demkov, D. G. Trabada, B. Haycock, H. Wang, G. Adams, J. K. Tomfohr, E. Abad, H. Wang, and D. A. Drabold, *Phys. Status Solidi (B) Basic Res.* **248**, 1989 (2011).
- [56] A. D. Becke, *Phys. Rev. A* **38**, 3098 (1988).
- [57] S. Grimme, S. Ehrlich, and L. Goerigk, *J. of Comput. Chem.* **32**, 1456 (2011).
- [58] M. A. Basanta, Y. J. Dappe, P. Jelínek, and J. Ortega, *Comput. Mater. Sci.* **39**, 759 (2007).
- [59] J. Bezanson, A. Edelman, S. Karpinski, and V. B. Shah, *SIAM Rev.* **59**, 65 (2017).
- [60] T. Michnowicz, B. Borca, R. Pétuya, V. Schendel, M. Pristl, I. Pentegov, U. Kraft, H. Klauk, P. Wahl, P. Mutombo, P. Jelínek, A. Arnau, U. Schlickum, and K. Kern, *Angewandte Chemie - International Edition* **59**, 6207 (2020).
- [61] C. Joachim, J. K. Gimzewski, R. R. Schlittler, and C. Chavy, *Phys. Rev. Lett.* **74**, 2102 (1995).

METHODS

Synthesis of molecular precursor. The detailed chemical synthesis procedure of precursor **1** and solution characterization data are shown in SCHEME. 2 and Fig. S13-Fig. S14.

Sample preparation and STM/STS Measurements. The STM experiments were conducted in UHV conditions (base pressure, $< 2 \times 10^{-9}$ mbar) at 4.4 K using a Scienta Omicron LT-STM system. Au(111) single crystal (MaTeck GmbH) was cleaned by multiple cycles of Ar⁺ sputtering (1×10^{-5} mbar) and annealing (710 K, 10 min). The precursor **1** was deposited from Knudsen cell (MBE-Komponenten GmbH) at 360 K onto clean Au(111) surface held at room temperature. After the deposition of the precursor molecules, the sample was annealed at 530 K for 20 min for the fabrication of OQCs. Subsequently, the sample was transferred into the STM/AFM head held at 4.5 K for STM imaging and characterization. All the BR-STM images were collected in constant height mode. The tip-sample distance with respect to an STM set point is indicated in the figure caption for each BR-STM image. The tip apex was functionalized with a CO molecule by picking up CO from Au(111) surface. The dI/dV spectra were collected using an internal lock-in amplifier with a modulation frequency of 693 Hz and amplitude of 20 mV. All the dI/dV maps were collected in a constant-current mode.

DFT simulations. The large scale total energy DFT calculations were performed using the Fireball package [55]. All geometry optimizations and electronic structure analyses were performed using BLYP exchange-correlation functional [56] with D3 corrections [57] and norm-conserving pseudopotentials with a basis set of optimized numerical atomic-like orbitals [58]. Atomic con-

682 figuration was allowed to relax until the remaining atomic⁷²⁶
 683 forces reached below $5 \times 10^{-2} \text{ eV\AA}^{-1}$. We employed slabs⁷²⁷
 684 model consisting of 60×60 unit cell of Au(111) surface⁷²⁸
 685 with 2 layers and 12-ring molecule, in total 1368 atoms.
 686 The last Au layer was kept fixed in the bulk position.
 687 Brillouin reciprocal zone was sampled by only Γ k-point.⁷²⁹
 688 The theoretical dI/dV simulations were carried out using
 689 probe particle STM code [40, 42] using electronic struc-⁷³⁰
 690 ture of free-standing 12-OQC. Metallic-tip was mimicked
 691 by s-like orbital without tip relaxation.

692 **QFT calculations.** The derivation of the field-
 693 theoretic formalism is provided in the Supplementary In-
 694 formation. The numerical calculations were performed
 695 using JULIA programming language [59].

der the supervision of A.R.; The manuscript was written
 by X.P., H.M., A.R. and J.L. with contributions from all
 co-authors.

COMPETING INTERESTS

The authors declare no competing interests.

DATA AVAILABILITY

697 The data that support the findings of this study are
 698 available from the corresponding authors on reasonable
 699 request.

CODE AVAILABILITY

701 The code used in the calculations is available at <https://github.com/rodin-physics/au-polymer>.
 702

ACKNOWLEDGMENTS

704 J.L. acknowledges support from MOE grants:
 705 MOE2019-T2-2-044 and R-143-000-B58-114. A.R.
 706 acknowledges the National Research Foundation, Prime
 707 Minister Office, Singapore, under its Medium Sized
 708 Centre Programme and the support by Yale-NUS
 709 College (through Grant No. R-607-265-380-121). P.M.
 710 and P.J. acknowledge support from the Praemium
 711 Academie of the Academy of Science of the Czech
 712 Republic and the CzechNanoLab Research Infrastruc-
 713 ture supported by MEYS CR (LM2018110). P.J.
 714 acknowledges the support of the GACR 20-13692X.
 715 P.M. acknowledges MSMT Project No. SOLID21 -
 716 CZ.02.1.01/0.0/0.0/16_019/0000760.

AUTHOR CONTRIBUTIONS

718 J.L. supervised the project. X.P. A.R., and J.L. con-
 719 ceived the project. X.P. performed experiments related
 720 to on-surface synthesis, STM/STS measurements, and
 721 data analysis. J.S., M.T., S.S., and P.L. assisted in the
 722 data analysis and contributed to the scientific discussion.
 723 S.D., P.N., J.W., C.C. designed and synthesized the pre-
 724 cursor molecules; P.M. and P.J. performed the DFT cal-
 725 culations; H.M. performed field theoretic calculations un-

731 SUPPLEMENTARY INFORMATION

732 Analytical Theory

733 To describe the Au(111) surface states, we employ the single-band nearly-free electron model with the dispersion
 734 $\varepsilon_{\mathbf{q}} = \hbar^2 |\mathbf{q}|^2 / (2m_e m^*)$, \mathbf{q} is the crystal momentum, m_e is the electron mass and $m^* = 0.27$ is the effective mass. The
 735 polymer induces a local potential so that the second-quantised Hamiltonian can be written as

$$\hat{\mathcal{H}} = \sum_{\mathbf{q}} c_{\mathbf{q}}^\dagger (\varepsilon_{\mathbf{q}} - \mu) c_{\mathbf{q}} + \sum_{\mathbf{r}} c_{\mathbf{r}}^\dagger U_{\mathbf{r}} c_{\mathbf{r}} = c_{\mathbf{Q}}^\dagger (H_{\mathbf{Q}} - \mu) c_{\mathbf{Q}} + c_{\mathbf{R}}^\dagger \mathbf{U} c_{\mathbf{R}}. \quad (1)$$

736 In the first term, $c_{\mathbf{q}}^\dagger (c_{\mathbf{q}})$ are fermionic creation (annihilation) operators associated with the single-band eigenstates
 737 and μ is the chemical potential. Because we are considering a single band, each unit cell at coordinate \mathbf{r} contains a
 738 single state whose creation (annihilation) operator is $c_{\mathbf{r}}^\dagger (c_{\mathbf{r}})$. $U_{\mathbf{r}}$ is the polymer-induced potential variation at \mathbf{r} . To
 739 make the expression more compact, we collect all $c_{\mathbf{q}}$ and $c_{\mathbf{r}}$ into vectors of operators $c_{\mathbf{Q}}$ and $c_{\mathbf{R}}$, respectively. From
 740 this, $H_{\mathbf{Q}}$ is a diagonal matrix of $\varepsilon_{\mathbf{q}}$, while \mathbf{U} is a diagonal matrix of $U_{\mathbf{r}}$.

741 Because $c_{\mathbf{R}}$ and $c_{\mathbf{Q}}$ are related by the unitary transformation $c_{\mathbf{R}} = \Theta c_{\mathbf{Q}}$, where $\Theta_{jk} = e^{i\mathbf{r}_j \cdot \mathbf{q}_k} / \sqrt{N}$ and N is the
 742 number of states in the system. This results in

$$\hat{\mathcal{H}} = c_{\mathbf{R}}^\dagger [\Theta (H_{\mathbf{Q}} - \mu) \Theta^\dagger + \mathbf{U}] c_{\mathbf{R}}. \quad (2)$$

743 This Hamiltonian can be transcribed into the imaginary-time action

$$S = \sum_{\omega_n} \bar{\phi}_n [\Theta (H_{\mathbf{Q}} - \mu - i\omega_n) \Theta^\dagger + \mathbf{U}] \phi_n, \quad (3)$$

744 where ϕ_n is a vector of Grassmann numbers corresponding to the fermionic operators and ω_n are the fermionic
 745 Matsubara frequencies. Exponentiating the action and integrating over the fields yields the partition function

$$\mathcal{Z} = \prod_{\omega_n} |\beta [\Theta (H_{\mathbf{Q}} - \mu - i\omega_n) \Theta^\dagger + \mathbf{U}]| = \prod_{\omega_n} |-\beta \Xi_{i\omega_n + \mu}^{-1} + \mathbf{U}| = \prod_{\omega_n} |-\beta G_{i\omega_n + \mu}^{-1}|, \quad (4)$$

746 where $G_{i\omega_n + \mu}$ is the full real-space Green's function, while $\Xi_{i\omega_n + \mu}$ is the same for a system without the polymer-
 747 induced potential perturbation \mathbf{U} and $\beta = 1/(k_B T)$. Explicitly,

$$G_{i\omega_n + \mu} = \Xi_{i\omega_n + \mu} + \Xi_{i\omega_n + \mu} \mathbf{U} (1 - \Xi_{i\omega_n + \mu} \mathbf{U})^{-1} \Xi_{i\omega_n + \mu}. \quad (5)$$

748 By taking the diagonal elements of $G_{i\omega_n + \mu}$ and replacing $i\omega_n \rightarrow \omega + i0^+$ allows us to write down the spectral
 749 function:

$$\mathcal{A}_\omega(\mathbf{r}_j) = -2\text{Im} \left[\Xi_{\omega + \mu} + \Xi_{\omega + \mu} \mathbf{U} (1 - \Xi_{\omega + \mu} \mathbf{U})^{-1} \Xi_{\omega + \mu} \right]_{jj}, \quad (6)$$

750 where the energy ω is measured from the Fermi level.

Note that at this point, Ξ and \mathbf{U} are $N \times N$ matrices. Naturally, as $N \rightarrow \infty$, the problem becomes intractable numerically. However, we now show that the expression simplifies considerably when one takes into account the structure of \mathbf{U} . We write

$$\left[\Xi_{\omega + \mu} + \Xi_{\omega + \mu} \mathbf{U} (1 - \Xi_{\omega + \mu} \mathbf{U})^{-1} \Xi_{\omega + \mu} \right]_{jj} = [\Xi_{\omega + \mu}]_{jj} + \sum_{klm} [\Xi_{\omega + \mu}]_{jk} \mathbf{U}_{kl} [1 - \Xi_{\omega + \mu} \mathbf{U}]_{lm}^{-1} [\Xi_{\omega + \mu}]_{mj}. \quad (7)$$

One can see here that k and l in the summation only include states that have non-vanishing elements in \mathbf{U} . In addition, expanding $[1 - \Xi_{i\omega_n + \mu} \mathbf{U}]_{lm}^{-1}$ as a geometric series, makes it clear that m also must correspond to a state with a finite elements in \mathbf{U} . This allows us to write

$$\left[\Xi_{\omega + \mu} + \Xi_{\omega + \mu} \mathbf{U} (1 - \Xi_{\omega + \mu} \mathbf{U})^{-1} \Xi_{\omega + \mu} \right]_{jj} = \Xi_{\omega + \mu}^{jj} + (\Xi_{\omega + \mu}^{j1} \quad \Xi_{\omega + \mu}^{j2} \quad \dots) \tilde{\mathbf{U}} \left(1 - \tilde{\Xi}_{\omega + \mu} \tilde{\mathbf{U}} \right)^{-1} \begin{pmatrix} \Xi_{\omega + \mu}^{1j} \\ \Xi_{\omega + \mu}^{2j} \\ \vdots \end{pmatrix}, \quad (8)$$

where the tilde indicates that only the unit cells with the potential perturbation are included and

$$\Xi_z^{jk} = \sum_{lm} [\Xi_z]_{jlk} = \sum_{lm} \Theta_{jl} (z - H_{\mathbf{Q}})_{lm}^{-1} \Theta_{mk}^\dagger = \sum_l \Theta_{jl} (z - H_{\mathbf{Q}})_{ll}^{-1} \Theta_{lk}^\dagger = \frac{1}{N} \sum_{\mathbf{q}} \frac{e^{i\mathbf{q}\cdot(\mathbf{r}_j - \mathbf{r}_k)}}{z - \varepsilon_{\mathbf{q}}}. \quad (9)$$

The momentum sum can be turned into an integral

$$\begin{aligned} \frac{1}{N} \sum_{\mathbf{q}} \frac{e^{i\mathbf{q}\cdot\mathbf{R}}}{z - \hbar^2 q^2 / (2m_e m^*)} &= \frac{A}{(2\pi)^2} \oint d\theta \int dq q \frac{e^{iqR \cos \theta}}{z - \text{Ry} \times a_0^2 q^2 / m^*} \\ &= \frac{1}{\text{Ry}} \frac{A}{2\pi} \int dq q \frac{J_0(qR)}{z/\text{Ry} - a_0^2 q^2 / m^*} = \frac{\sqrt{m^*}}{\text{Ry}} \frac{A/a_0^2}{2\pi} \int du u \frac{J_0(\sqrt{m^*} u R / a_0)}{z/\text{Ry} - u^2}, \end{aligned} \quad (10)$$

751 where K_0 is the modified Bessel function, A is the area of the unit cell, Ry is the Rydberg energy, and a_0 is the Bohr
752 radius.

753 If $R \neq 0$, we set the limits of u integration as $[0, \infty)$ to yield

$$\Xi_z^{R \neq 0} = \frac{\sqrt{m^*}}{\text{Ry}} \frac{\tilde{A}}{2\pi} \int_0^\infty du u \frac{J_0(\sqrt{m^*} u \tilde{R})}{z/\text{Ry} - u^2} = -\frac{\sqrt{m^*}}{\text{Ry}} \frac{\tilde{A}}{2\pi} K_0 \left(\sqrt{m^*} \tilde{R} \sqrt{-\frac{z}{\text{Ry}}} \right), \quad (11)$$

754 where $\tilde{A} = A/a_0^2$ and $\tilde{R} = R/a_0$.

755 For $R = 0$, the integral diverges and we introduce a cutoff so that $u \in [0, \sqrt{C}]$ so that

$$\Xi_z^{R=0} = \frac{\sqrt{m^*}}{\text{Ry}} \frac{\tilde{A}}{2\pi} \int_0^{\sqrt{C}} du \frac{u}{z/\text{Ry} - u^2} = -\frac{1}{2} \frac{\sqrt{m^*}}{\text{Ry}} \frac{\tilde{A}}{2\pi} \ln \left(1 - \frac{C}{z/\text{Ry}} \right). \quad (12)$$

756 As the final step, we determine the value of C . Using the fact that $-2\text{Im}[\Xi_{\omega+i0}^{R=0}]$ is the spectral function for the
757 pristine system whose integral on $\omega \in (-\infty, \infty)$ yields 2π , we get

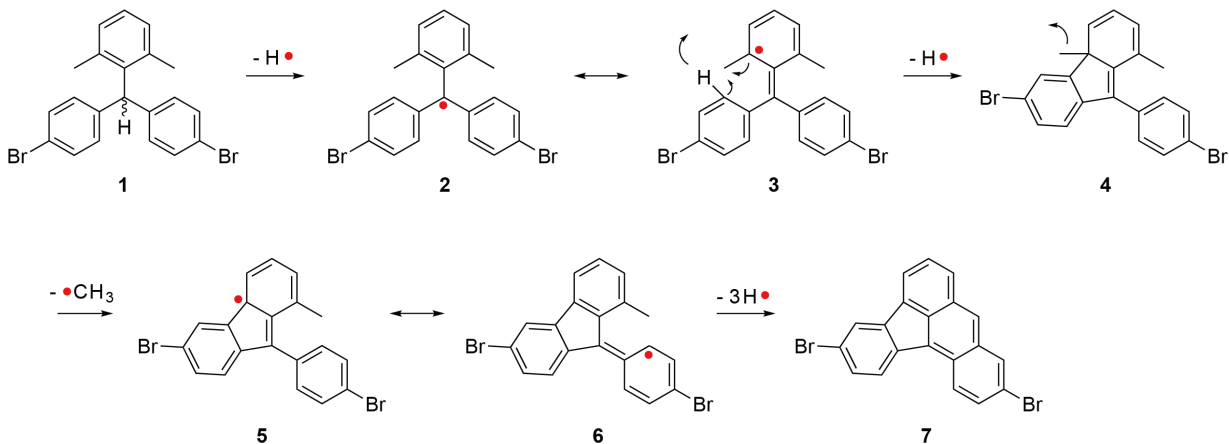
$$\int_{-\infty}^{\infty} d\omega \text{Im} \left[\frac{\sqrt{m^*}}{\text{Ry}} \frac{\tilde{A}}{2\pi} \ln \left(1 - \frac{C \times \text{Ry}}{\omega + i0} \right) \right] = \frac{\sqrt{m^*}}{\text{Ry}} \frac{\tilde{A}}{2\pi} \times C \times \text{Ry} \times \pi \quad (13)$$

758 leading to $C = \frac{4\pi}{A\sqrt{m^*}}$. This yields

$$\begin{aligned} \Xi_z^{R \neq 0} &= -\frac{2}{C\text{Ry}} K_0 \left(\sqrt{m^*} \tilde{R} \sqrt{-\frac{z}{\text{Ry}}} \right), \\ \Xi_z^{R=0} &= -\frac{1}{C\text{Ry}} \ln \left(1 - \frac{C\text{Ry}}{z} \right). \end{aligned} \quad (14)$$

759 **Supplementary note 1. Proposed mechanism of the formation of pentagonal ring.**

760 The precursor **1** is expected to undergo the thermally-triggered dehydrogenation, leading to the formation of one
761 radical at the central methylene (**2**). It can be delocalized to dimethylphenyl site for the subsequent bonding with
762 bromophenyl ring to form pentagonal ring (from **3** to **6**) via demethylation. A further dehydrogenation on the other
763 methyl group and the other bromophenyl generates planar **7**. The high chemical activity of monoradical **2** is expected
764 to be the driving force towards the formation of closed-shell compound **7** with planar structure [39].



SCHEME 1. Proposed reaction pathway for the formation of pentagonal ring via the demethylation

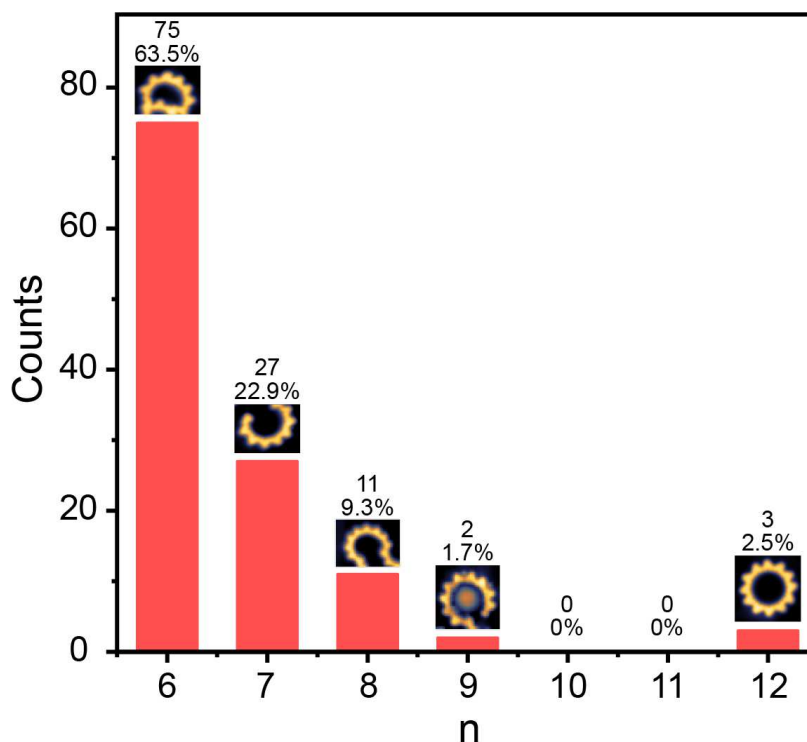


FIG. S1. Statistic analysis of regular curved ring segments with different numbers (n) of building units (regular curved ring segments and complete rings with $n > 12$ were not observed).

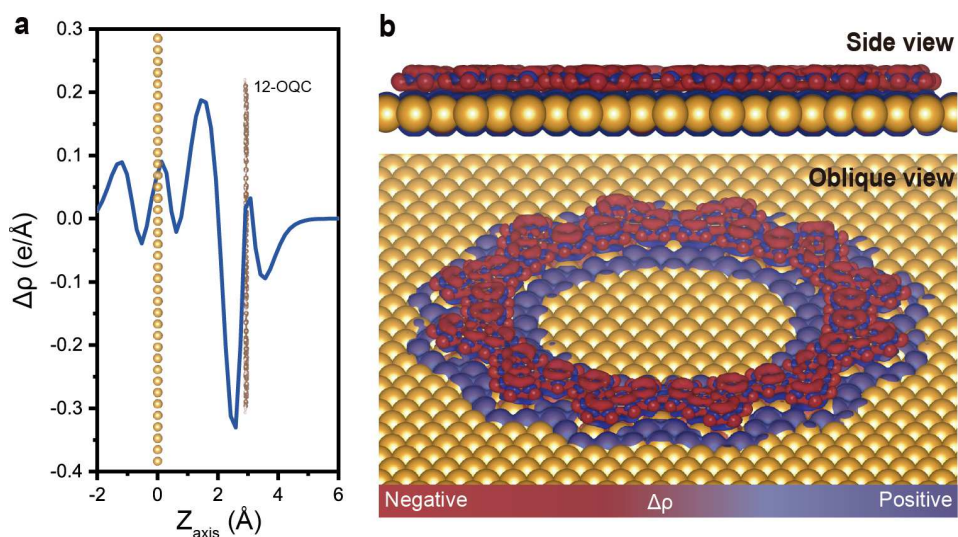


FIG. S2. **DFT-calculated charge redistribution of a 12-OQC on Au(111).** **a**, Projection of the charge redistribution of 12-OQC on Au(111) along the z -axis ($\Delta\rho = \rho_{\text{total}} - \rho_{\text{surface}} - \rho_{\text{molecule}}$). **b**, 3D isosurface of the electronic density differences with an isovalue of $\pm 0.001 \text{ e}/\text{\AA}^3$ of 12-OQC on Au(111) surface (upper panel and bottom panel are side and oblique view, respectively). Red and purple regions in 3D plots represent charge depletion and accumulation, respectively.

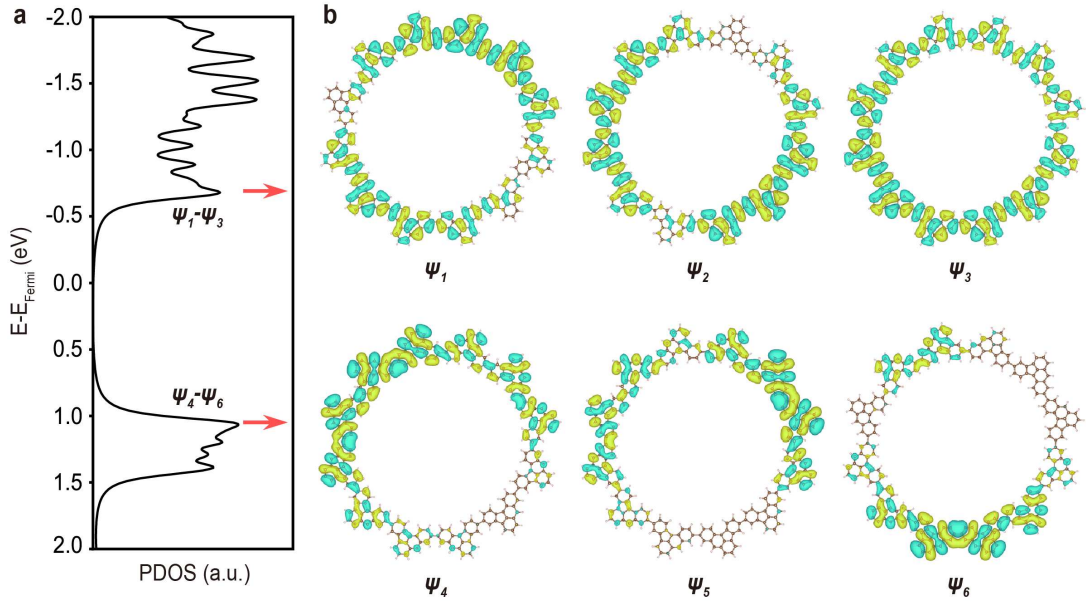


FIG. S3. **Orbital structure of a freestanding 12-OQC.** **a**, The projected density of states (PDOS) of 12-OQC calculated by BLYP functional. **b**, Spatial distribution of ψ_{1-6} orbitals of 12-OQC.

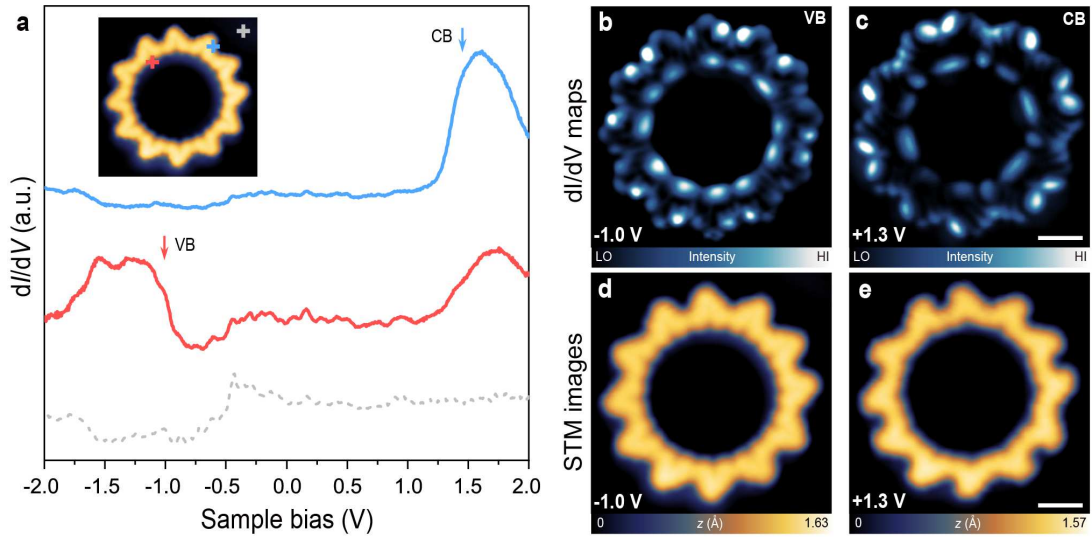


FIG. S4. **Electronic structure characterization of a second 12-OQC.** **a**, Point dI/dV spectra acquired over different sites of 12-OQC and Au(111) substrate. dI/dV curves taken at the pentagonal ring (blue curve), inner edge of 12-OQC (red curve), and taken on Au(111) (grey dashed curve). **b,c**, Constant-current dI/dV maps recorded at the energy positions of the VB (-1.0 V) and CB ($+1.3$ V) of 12-OQC, respectively. **d,e**, The corresponding STM images of **b,c** collected simultaneously with constant current dI/dV maps ($I = 2$ nA for **b-e**). Scale bar: 1 nm.

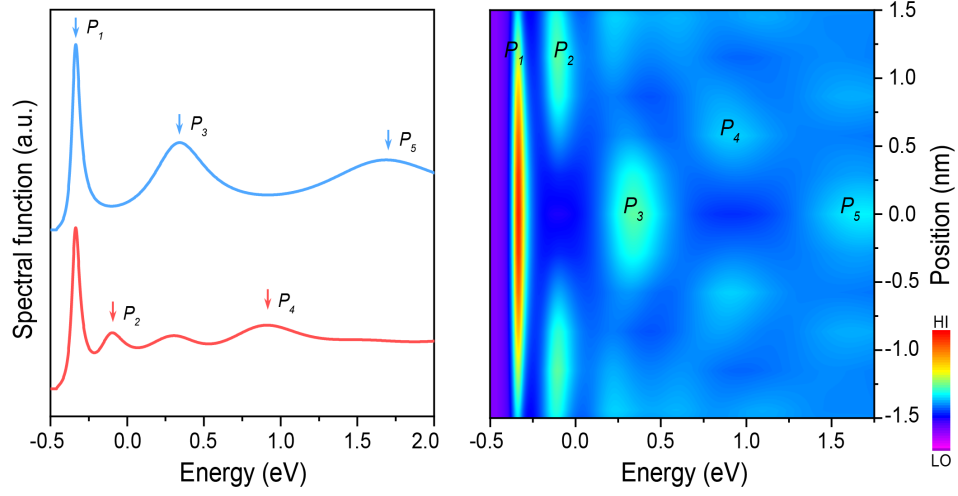


FIG. S5. Calculated position-dependent spectral function over different sites inside 12-OQC (left). Blue and red curve taken at the centre and 0.6 nm away from the centre of simulated model. Color-coded simulated spectral function curves (spaced by 0.15 nm) taken across the pore of potential corral in gold unit cells (right).

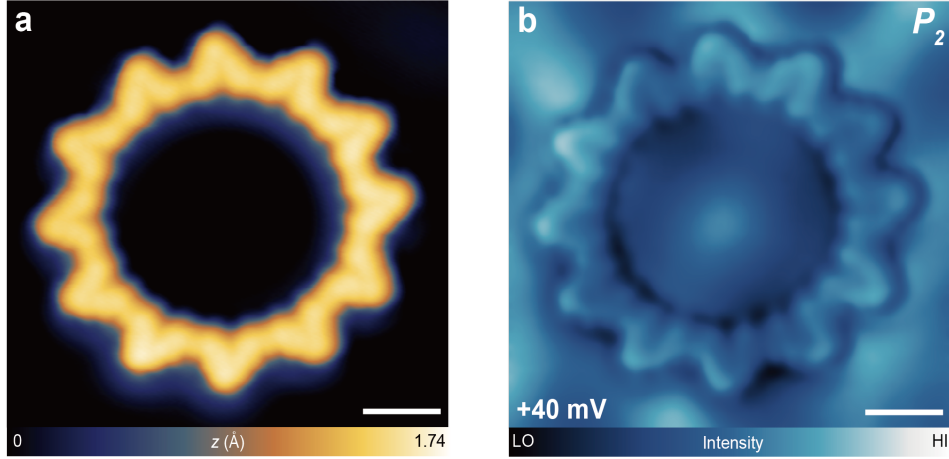


FIG. S6. **Resonance state (P_2) inside the 12-OQC.** **a**, The corresponding STM image of **b** collected simultaneously with constant-current dI/dV map ($V = +40$ mV, $I = 1$ nA) of 12-OQC. **b**, Constant-current dI/dV map recorded at +40 mV. Scale bar: 1 nm.

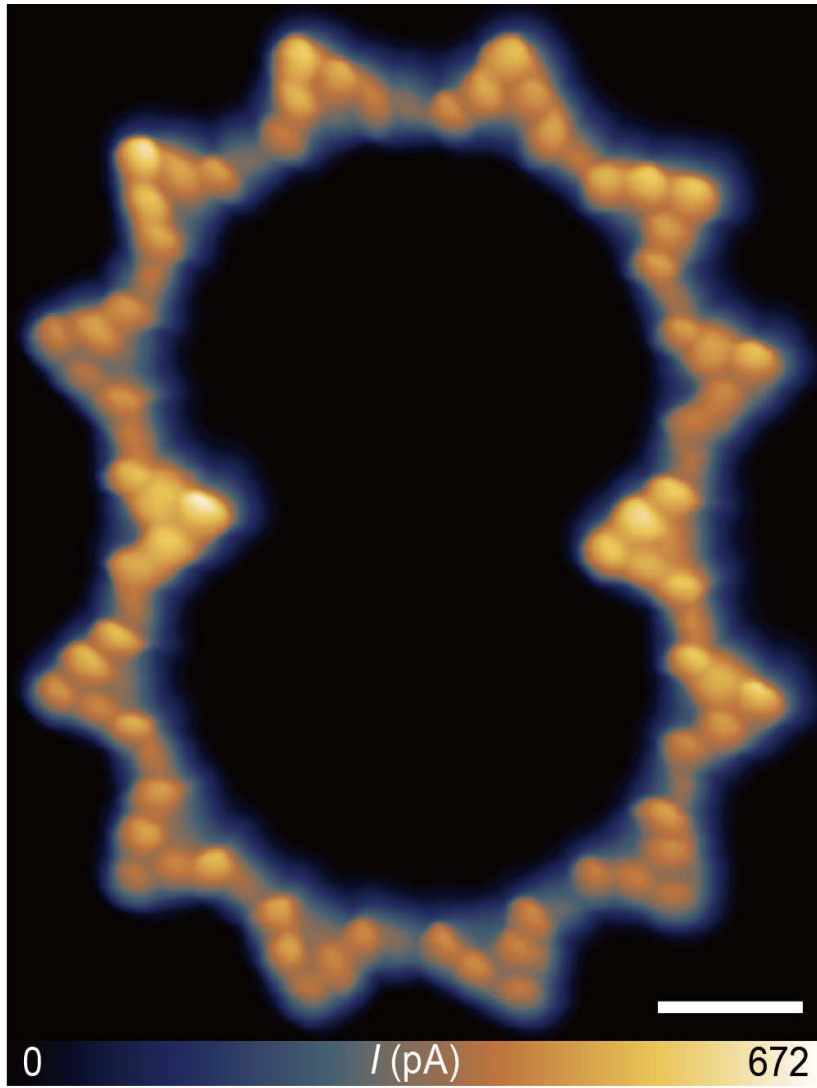


FIG. S7. BR-STM image of a symmetric COS-OQC ($V = 10$ mV, $\Delta z = -1.5$ Å; set point prior to turn off feedback, $V = 20$ mV, $I = 600$ pA). Scale bar: 1 nm.

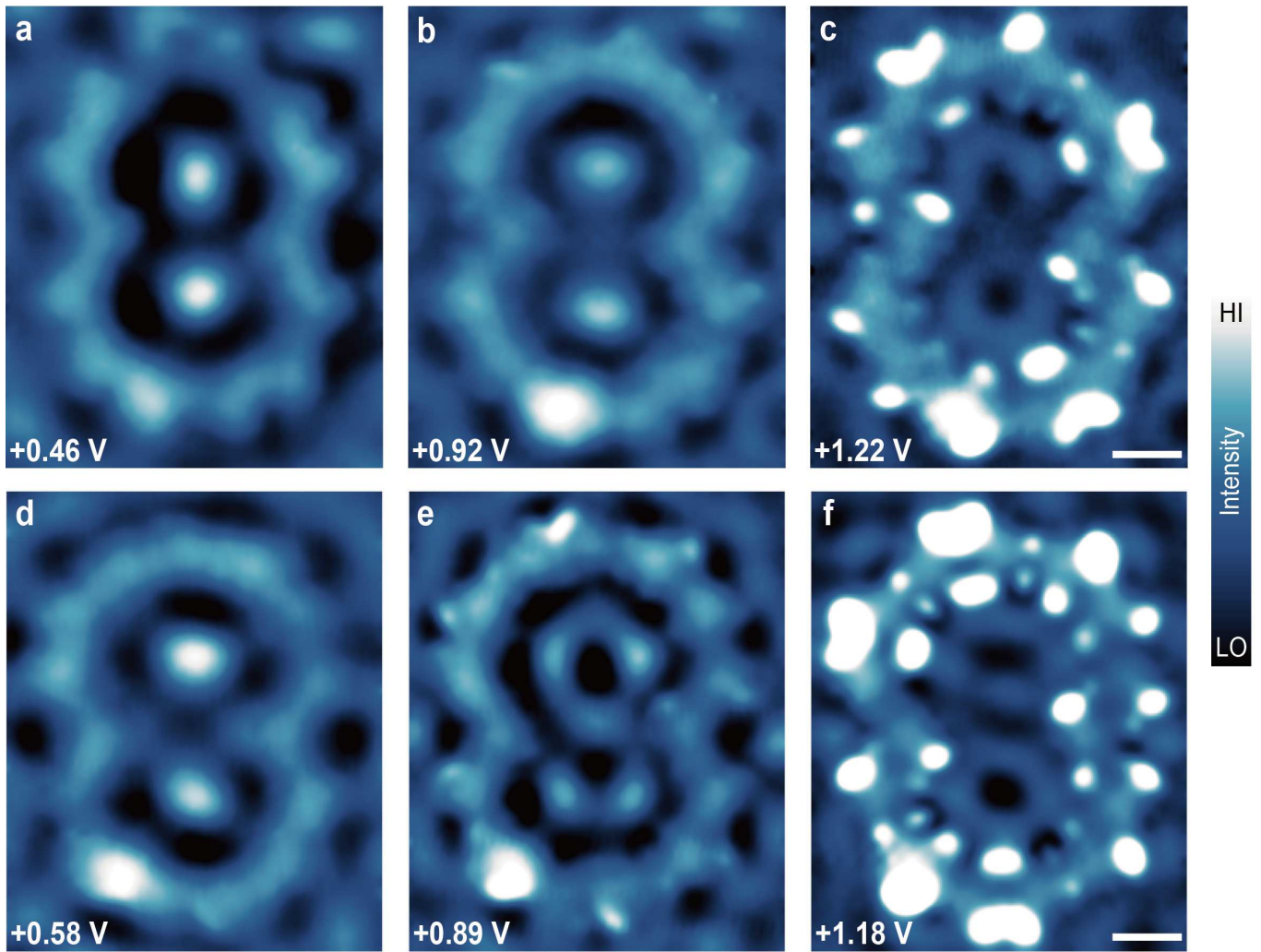


FIG. S8. **Characterization of quantum resonance states in symmetric and asymmetric COS-OQC.** **a-c**, Constant-current dI/dV maps of a symmetric COS-OQC recorded at different energy positions ($I = 1$ nA for **a**; $I = 1.5$ nA for **b,c**). **d-f**, Constant-current dI/dV maps of an asymmetric COS-OQC recorded at different energy positions ($I = 1$ nA for **d**; $I = 1.5$ nA for **e,f**). Scale bar: 1 nm.

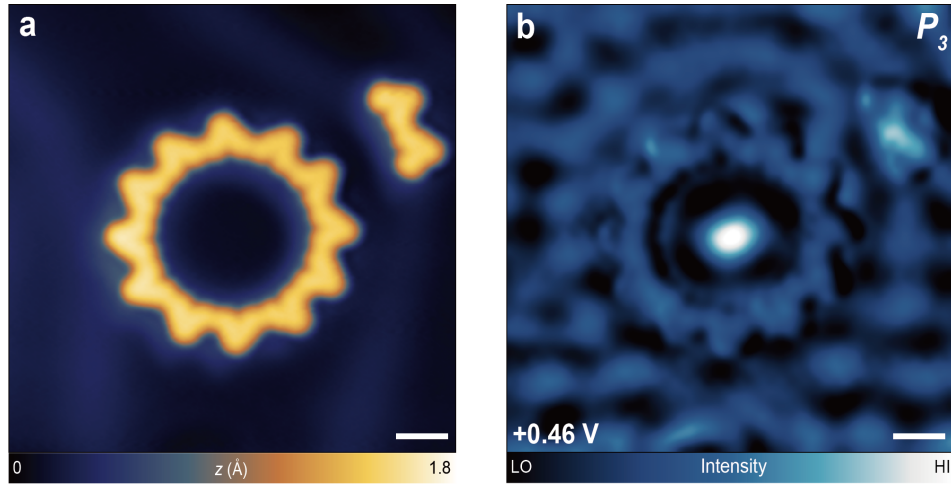


FIG. S9. **Scattered wave patterns surrounding the 12-OQC.** **a**, The corresponding STM image of **b** collected simultaneously with constant-current dI/dV map ($V = +0.46$ V, $I = 1.2$ nA) of 12-OQC. **b**, Constant-current dI/dV map recorded at +0.46 V (P_3). Scale bar: 1 nm.

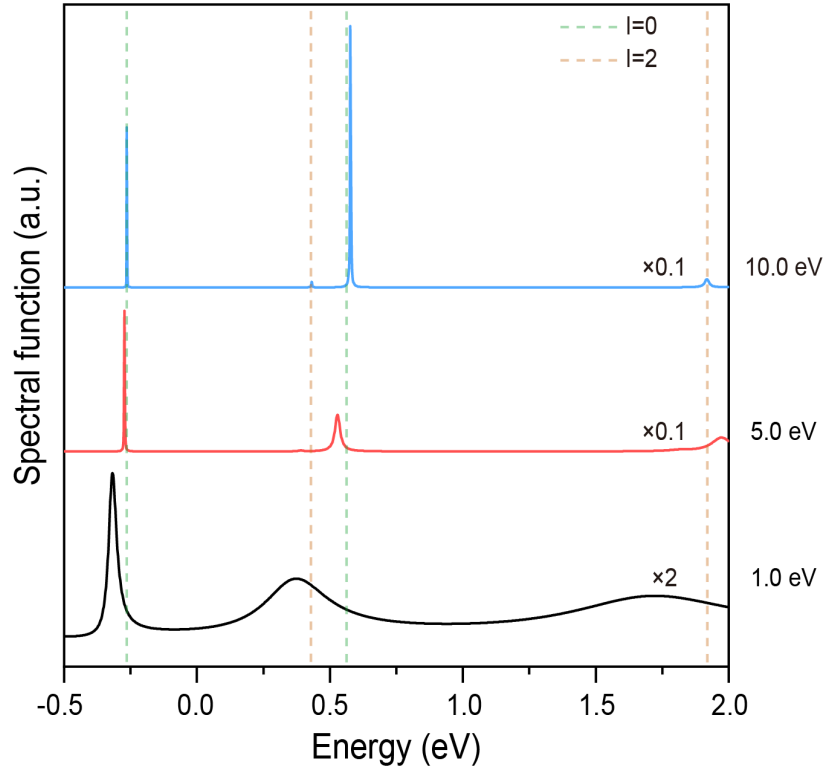


FIG. S10. **Comparison between resonance states in quantum corrals with different barrier heights and bound states.** Calculated spectral function curves taken at the centre of simulated 12-OQC model with barrier heights of 1.0 eV (black curve), 5.0 eV (red curve) and 10.0 eV (blue curve), respectively. The dashed lines present the energy positions of bound states in the quantum well with the same geometry when the angular momentum $l = 0$ (green dashed lines) and 2 (orange dashed lines).

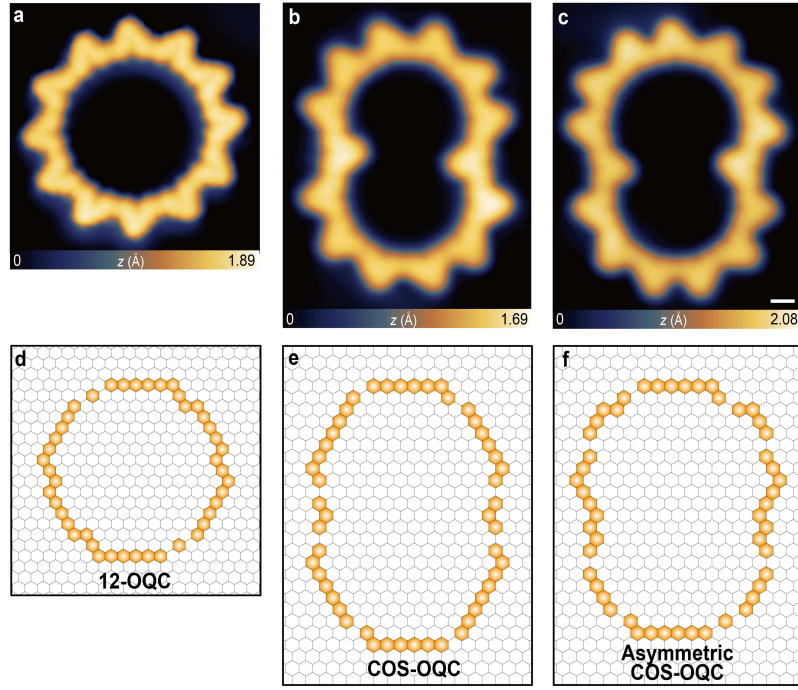


FIG. S11. **The positions of repulsive potential scatters placed over Au unit cells.** **a**, STM image of 12-OQC ($V = -0.26$ V, $I = 1$ nA). **b**, STM image of a symmetric COS-OQC ($V = -0.32$ V, $I = 1.5$ nA). **c**, STM image of an asymmetric COS-OQC ($V = -0.3$ V, $I = 1.5$ nA). **d-f**, Corresponding simulation models of repulsive potential scatter placed over Au unit cells for 12-OQC, COS-OQC and asymmetric COS-OQC, respectively (the unit cells in orange color indicate the positions where we included the repulsive potential scatters). Scale bar: 5 \AA .

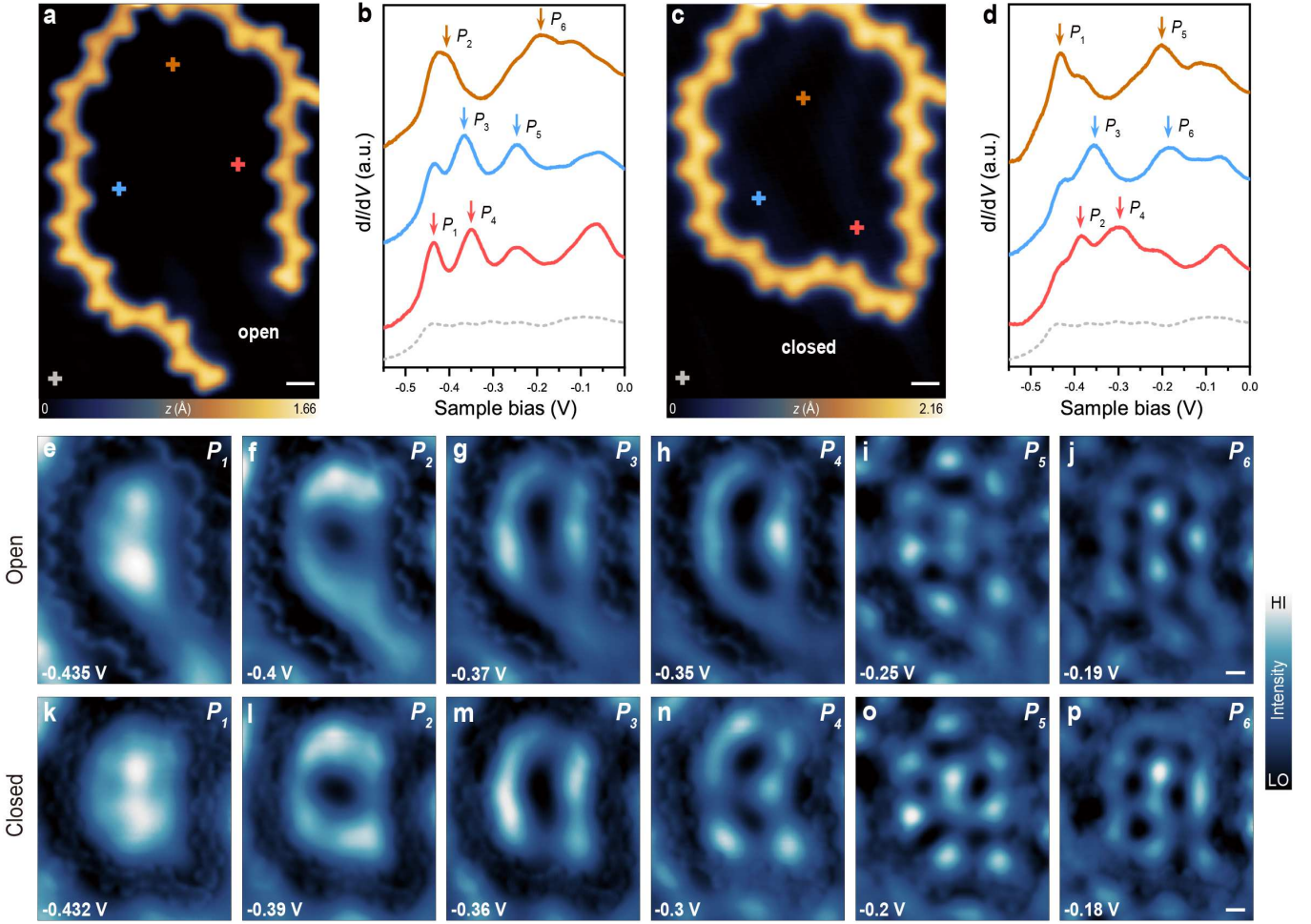
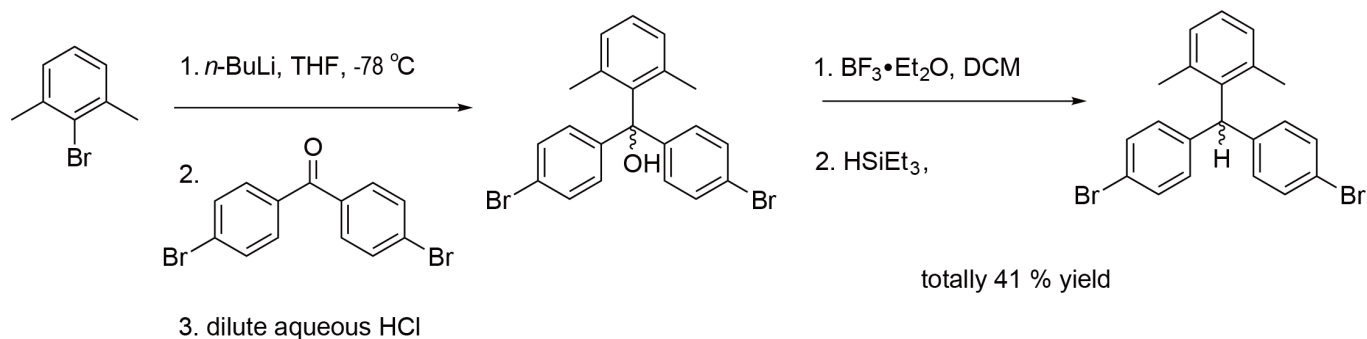


FIG. S12. **Control the geometries of OQC via tip manipulation to tune their resonance states.** **a**, STM image of open OQC before manipulation ($V = -0.37$ V, $I = 1$ nA). **b**, Point dI/dV spectra acquired over different sites of OQC and Au(111) substrate. dI/dV curves taken at the position of red cross in **a** (red curve), blue cross in **a** (blue curve), orange cross in **a** (orange curve), and taken on Au(111) (grey dashed curve). **c**, STM image of closed OQC after manipulation ($V = -0.432$ V, $I = 1$ nA). **d**, Point dI/dV spectra acquired over different sites of closed OQC and Au(111) substrate. dI/dV curves taken at the position of red cross in **c** (red curve), blue cross in **c** (blue curve), orange cross in **c** (orange curve), and taken on Au(111) (grey dashed curve). **e-j**, Constant-current dI/dV maps recorded at the energy positions of the P_1 (-0.435 V), P_2 (-0.4 V), P_3 (-0.37 V), P_4 (-0.35 V), P_5 (-0.25 V) and P_6 (-0.19 V) of OQC, respectively ($I = 1$ nA for **e-h**; $I = 800$ pA for **i,j**). **k-p**, Constant-current dI/dV maps recorded at the energy positions of the P_1 (-0.432 V), P_2 (-0.39 V), P_3 (-0.36 V), P_4 (-0.3 V), P_5 (-0.2 V) and P_6 (-0.18 V) of closed OQC, respectively ($I = 1$ nA for **k-n**; $I = 800$ pA for **o,p**). Scale bar: 1 nm.

Supplementary note 2. Tuning the quantum resonance states via tip manipulation.

To conduct tip manipulation [60, 61], we first positioned the STM tip over the terminus of OQC with a set point of $V = 1$ mV, $I = 100$ pA and then switched off the feedback loop. The tip-sample distance was subsequently reduced by 1.5 Å, at which an abrupt increase in tunnelling current occurs, suggesting the contact of tip apex with the terminus of OQC. After retracting the tip by 200 pm, a controllable STM lateral manipulation was conducted by moving the tip along a defined trajectory (Fig. S12c). We then performed dI/dV measurements to probe the resonance states before and after tip manipulation. As shown in Fig. S12b,d, a series of resonance states were revealed in the corresponding dI/dV spectra acquired at the positions indicated by the crosses with different colors in Fig. S12a,c, which are labelled as P_1 - P_6 from low energy to high energy. We then carried out dI/dV mapping to probe the spatial distribution of these resonance states. By comparing the patterns of dI/dV maps of original OQC in Fig. S12e-j with their corresponding dI/dV maps after manipulation in Fig. S12k-p, the similar hot spots (P_1 , P_5 and P_6) and ring-like features (P_2 , P_3 and P_4) observed in these two OQCs suggest they are originated from the same resonance state. As expected, the energetic positions of these states all shift to higher energy after tip manipulation. This is because a smaller size of corral after tip manipulation is expected to produce the quantum resonance states at high

779 energy position. This proves that quantum states in OQCs could be further engineered *via* tip manipulation.



SCHEME 2. Synthetic route of precursor 1

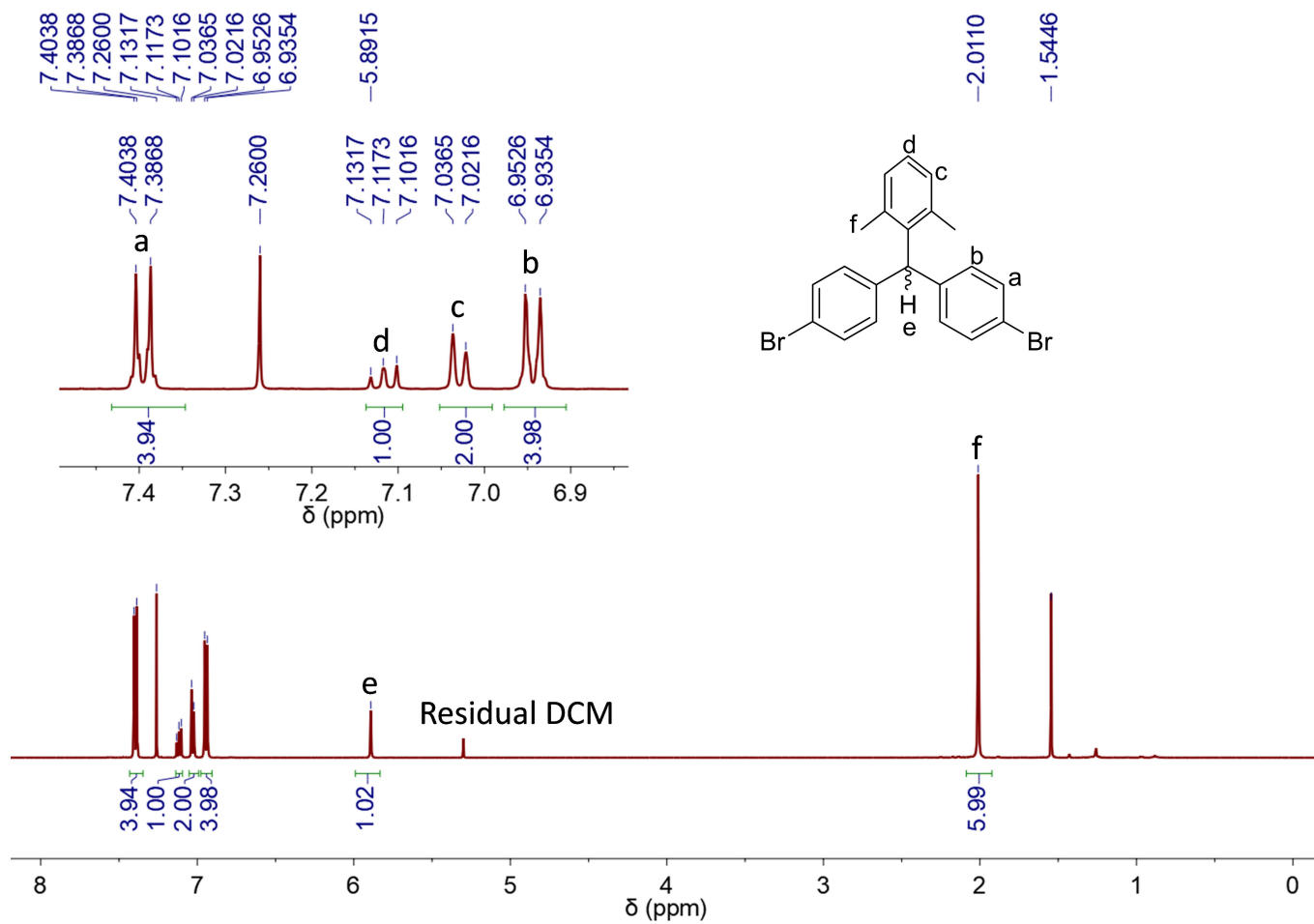
Synthetic route.

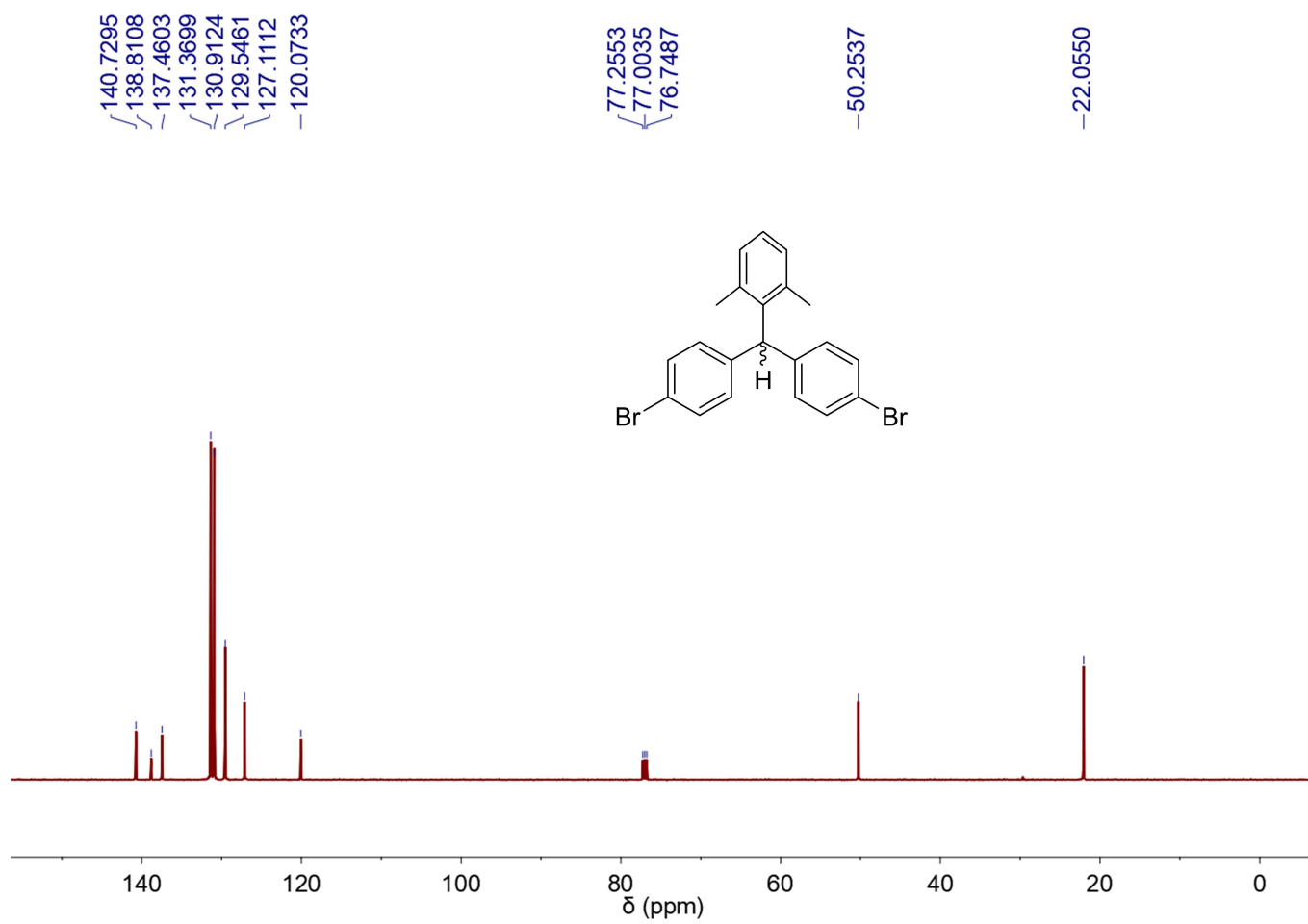
780 **Synthetic route.**
 781 *n*-BuLi (1.0 ml, 2.0 mmol, 2M) was added dropwise into the solution of 2-bromo-1,3-dimethylbenzene (0.30 ml,
 782 2.2 mmol) in dry THF (20 ml) at -78 °C, and the solution was stirred at this temperature for 2 hrs. Then, bis(4-
 783 bromophenyl)methanone (750 mg, 2.2 mmol) was added into the solution. After stirring for 2 hrs at -78 °C, the
 784 mixture was gradually warmed up to room temperature. Another 2 hrs later, dilute aqueous HCl solution (5 ml, 1M)
 785 was added to quench the reaction. Then, diethyl ether (30 ml) was added and the organic layer was washed with brine
 786 for three times and dried over anhydrous sodium sulfate. The crude product was directly used for next step after
 787 evaporating off the solvent. The crude product was dissolved in dry dichloromethane (DCM, 30 ml), and $\text{BF}_3 \cdot \text{Et}_2\text{O}$
 788 (0.30 ml, 2.3 mmol) was added into the solution. 30 mins later, triethylsilane (0.35 ml, 2.2 mmol) was dropwise into
 789 the mixture. 1 hr later, the reaction was quenched with triethylamine (0.5 ml) and the solution was washed with
 790 brine for three times and dried over anhydrous sodium sulfate. After removing the solvent, the crude product was
 791 purified by column chromatography with DCM/hexane as eluent (1/8, v/v) to afford precursor 1 (350 mg) in 41%
 792 yield.

793 $^1\text{H NMR}$ (500 MHz, CDCl_3): δ (ppm) 7.40 (d, $J = 8.5$ Hz, 4H), 7.12 (t, $J = 7.5$ Hz, 1H), 7.03 (d, $J = 7.5$ Hz,
 794 2H), 6.94 (d, $J = 8.6$ Hz, 4H), 5.89 (s, 1H), 2.01 (s, 6H);

795 $^{13}\text{C NMR}$ (125 MHz, CDCl_3): δ 140.73, 138.81, 137.46, 131.37, 130.91, 129.55, 127.11, 120.07, 50.25, 22.06.

796 **HRMS** analysis (EI): calcd for $\text{C}_{19}\text{H}_{15}\text{NBr}$ (M) $^+$: 427.9777; found: 427.9775 (error: 1.17 ppm).

FIG. S13. ^1H NMR spectrum of precursor **1** (500 MHz, CDCl_3).

FIG. S14. ^{13}C NMR spectrum of precursor 1 (125 MHz, CDCl_3).

Mass Spectrum SmartFormula Report

| | | | |
|------------------------|----------------------|-------------------------------|----------------------------------|
| Sample Name | 1 | Data File | D:\Chem\2021\202104\20210416\1.D |
| Instrument Name | Agilent 7200 GC-QTOF | IRM Calibration Status | Success |
| Acq Method | EIHR_CalValve.ei.m | Acquired Time | 16/4/2021 3:13:11 PM (UTC+08:00) |
| Comment | A/P Chi Chunyan | Operator | |

| Meas. m/z | # | Formula | Calc. Mass | Err [ppm] |
|-----------|---|--|------------|-----------|
| 427.9775 | 1 | C ₂₁ H ₁₈ [⁷⁹ Br] ₂ | 427.977 | 1.17 |

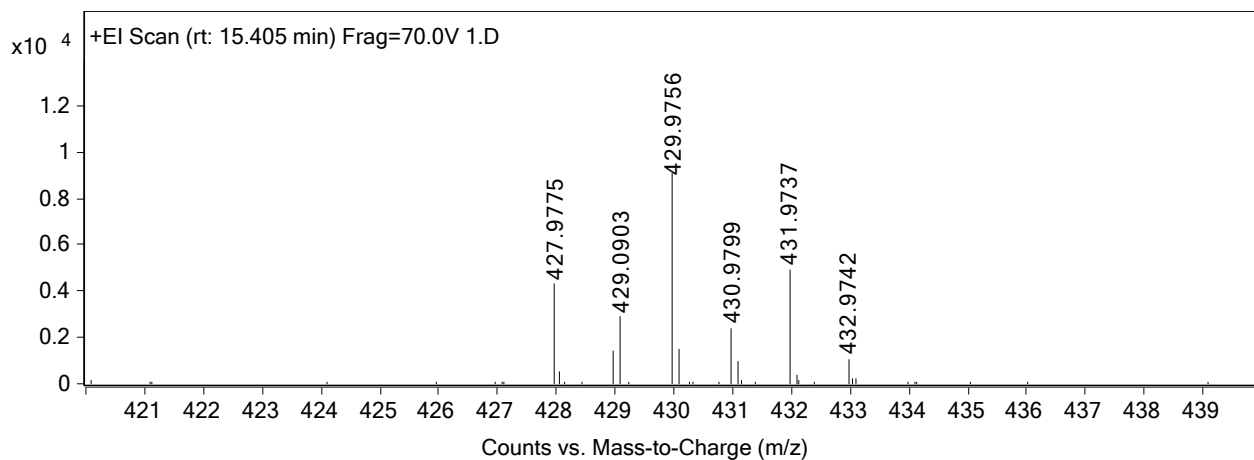


FIG. S15. HR mass spectrum (EI) of precursor 1.